Refractory solid condensation detected in an embedded protoplanetary disk

M. K. McClure[1*], Merel van 't Hoff[2,3], Logan Francis[1], Edwin Bergin[2], Will R. M. Rocha[1,4], J. A. Sturm[1], Daniel Harsono[5], Ewine F. van Dishoeck[1], John H. Black[6], J. A. Noble[7], D. Qasim[8], E. Dartois[9]

[1]Leiden Observatory, Leiden University, PO Box 9513, NL–2300 RA Leiden, The Netherlands.
[2]Department of Astronomy, The University of Michigan, 1085 S University Ave, Ann Arbor, MI 48109, USA.
[3]Purdue University, Department of Physics and Astronomy, 525 Northwestern Avenue, West Lafayette, IN 47907, USA.
[4]Laboratory for Astrophysics, Leiden Observatory, Leiden University, PO Box 9513, NL–2300 RA Leiden, The Netherlands.
[5]Institute of Astronomy, Department of Physics, National Tsing Hua University, Hsinchu, Taiwan.
[6]Chalmers University of Technology, Department of Space, Earth and Environment, Onsala Space Observatory, 439 92 Onsala, Sweden.
[7]Physique des Interactions Ioniques et Moléculaires, CNRS, Aix Marseille Université, Marseille, France.
[8]Southwest Research Institute, San Antonio, TX, USA.
[9]Institut des Sciences Moléculaires d'Orsay, CNRS, Université Paris-Saclay, Orsay, France.

*Corresponding author(s). E-mail(s): mcclure@strw.leidenuniv.nl;
Contributing authors: mervth@umich.edu; francis@strw.leidenuniv.nl; ebergin@umich.edu; rocha@strw.leidenuniv.nl; sturm@strw.leidenuniv.nl ; dharsono@gapp.nthu.edu.tw; ewine@strw.leidenuniv.nl; john.black@chalmers.se; jennifer.noble@univ-amu.fr; danna.qasim@swri.org; emmanuel.dartois@universite-paris-saclay.fr;

Abstract

Terrestrial planets and small bodies in our Solar System are theorized to have assembled from interstellar solids mixed with rocky solids that precipitated from a hot, cooling gas[1, 2]. The first high-temperature minerals to re-condense from this gaseous reservoir start the clock on planet formation[3, 4]. However, the production mechanism of this initial hot gas and its importance to planet formation in other systems are unclear. We report here the astronomical detection of this t=0 moment, capturing the building blocks of a new planetary system beginning its assembly. The young protostar HOPS-315 is observed at infrared and millimeter wavelengths with the James Webb Space Telescope (JWST) and the Atacama Large Millimeter Array (ALMA), revealing a reservoir of warm silicon monoxide gas and crystalline silicate minerals low in the atmosphere of a disk within 2.2 au of the star, physically isolated from the millimeter SiO jet. Comparison with condensation models with rapid grain growth and disk structure models suggests the formation of refractory solids analogous to those in our Solar System. Our results indicate that the environment in the inner disk region is influenced by sublimation of interstellar solids and subsequent refractory solid re-condensation from this gas reservoir on timescales comparable to refractory condensation in our own Solar System.

Keywords: Planet formation, Solar System, Accretion physics, Astrochemistry

1 Introduction & Results

The Class I protostar HOPS-315, located in the Orion B Molecular Cloud at a distance of 420 pc [5–7], is an ideal target for studying the formation of the first refractory solids in other star systems. As shown in Fig. 1, it has a clear, 40° sightline through its embedding, dusty envelope to a gaseous disk accreting onto the central protostar [5, 8–10]. The energy released by such accretion can heat the disk midplane to the point where rocky grains vaporize near ∼1300 K [11, 12], potentially resetting the interstellar dust composition to molecular and atomic gas from which only the most refractory solids can re-condense [13, 14].

Our Cycle 1 General Observer program with JWST (Program 1854, principal investigator (PI) M.K̃. McClure) observed HOPS-315 using the integral field spectroscopy (IFU) modes of the near-infrared spectrograph (NIRSpec) and mid-infrared instrument (MIRI) with high signal-to-noise-ratio (SNR∼540 at 8 μm; Methods). The high spectral resolution of these instruments reveals a rich spectrum dominated by strong absorption features of icy and rocky solids and copious gas phase species (Fig. 2). Unusually, we detect both the SiO vibrational fundamental gas band and crystalline SiO-rich solids (silicates) in absorption. The strength of the latter is unusual for protostars [15], although similarly prominent features towards another protostar [16] were attributed to crystalline grains entrained in an outflow.

Although HOPS-315 indeed sports a prominent H_2 jet and disk wind ([17], [18]), they likely do not carry the observed crystalline silicates. First, HOPS-315's jet is not detected in extended Fe^+ emission, a common infrared tracer [19–23], even at knots where entrained dust grains should sputter, suggesting the jet contains little dust. Second, HOPS-315's H_2 must emit from a hot *foreground* layer, while its crystalline dust must absorb in a cooler layer above a hot *background* layer. This absorbing layer is sandwiched *below* the hot H_2 emitting layer, since the 9.66μm H_2 0-0 S(3) line, in the bottom of the silicate absorption complex, has a visibly higher peak-to-continuum ratio than the H_2 0-0 S(2) line outside of the silicate band, implying that the silicates do not extinct the S(3) emission. Such vertically layered temperature 'inversion' patterns are predicted for disks around highly accreting stars. High-pressure, radially extended 'thermostat' regions develop at their midplanes, maintaining equilibrium between silicate vaporization and re-condensation at T_{sil} ~1300 K [11–13], resulting in local SiO gas and crystalline silicate production, respectively [24]. *This previously undetected thermostat region has been proposed as a point of origin for refractory solids in the Solar System [13, 14].*

We test whether the observed crystalline silicates and SiO gas are consistent with production under such physical conditions. First, we fit laboratory mineral data to the solid-state absorption features between 7.75–28 μm (Methods, and Extended Data Table 1), identifying forsterite (Mg_2SiO_4, $N_{\rm forst}=1.3^{+0.5}_{-0.8}\times10^{17}$ cm^{-2}) and enstatite ($MgSiO_3$, $N_{\rm enst}=3.7^{+0.6}_{-0.8}\times10^{17}$ cm^{-2}) robustly (Fig. 3). Silica (SiO_2, $N_{\rm silica}=1.4^{+0.2}_{-0.1}\times10^{17}$ cm^{-2}) is tentatively detected at a 3σ level (see significance discussion in Methods). The abundance ratio of $N_{enstatite}/N_{forsterite}$ is high at $2.8^{+5.8}_{-1.2}$. Next, we next measure the temperature, column density, and line width of all observed molecular gas species using slab models of line optical depths (Methods, Extended Data Table 2). The line width implies a rough constraint on each molecule's location. In the absence of strong turbulence, infrared SiO absorbs near 1 au with a column density of $N_{\rm SiO}=4.62\pm0.14\times10^{18}$ cm^{-2} and temperature $T_{SiO}=472^{+6}_{-4}$ K, well below the silicate sublimation temperature. Cross-correlating our SiO model with the observed molecular band indicates a velocity of -10.6±1.2 km s^{-1}, which is blueshifted by ~20 km s^{-1} from the millimeter system velocity of +9.68±0.19 km s^{-1} (all in the velocity reference frame of the kinematic local standard of rest, v_{LSRK}; Methods, Extended Data Figure 1). This velocity suggests that the infrared SiO gas is flowing upward from the thermostat region into the cooler inversion layer, where the crystalline silicates are absorbing below the H_2 emitting disk wind [i.e. discussion of H_2 S(3) line above, 18], rather than in the known molecular jet [17, 25].

The other absorbing molecular gas species map the spatial gradients in temperature and column density of the cooler absorbing layer that is sandwiched between the hot midplane and hot, H_2 emitting disk surface (see Fig. 1, Extended Data Table 2, and Methods). The pattern of radial locations for each molecular band and the values for their temperatures broadly agree with expectations from 2D disk models for similar bands in emission [26]. The bands with moderate optical depth (e.g SiO, 17μm H_2O) must arise just above the disk photosphere, where the optical depth is 2/3 [11].

Similar to the Sun's atmosphere, the disk photosphere must be located below the temperature minimum, to explain the absorption lines [27]. The detection of the 4.7 μm absorption band of ^{12}CO at 1181 K implies a midplane temperature >1200 K, matching predictions of the thermostat region from disk structure models [12, 14], cementing our identification.

To confirm that the SiO absorbing region and SiO jet are separate, we requested high angular resolution (10 au beamsize) ALMA observations of SiO, ^{12}CO, and SO through a Director's Discretionary Time (DDT) proposal (PI M. van't Hoff, Methods). The millimeter SiO spectrum also shows only jet velocity components at -80 km s^{-1} and $+100$ km s^{-1}, and no slower component around the infrared SiO velocity of -10.6$\pm$1.2 km s^{-1} (Fig. 4), confirming that the infrared SiO is not tracing the jet. Finally, the blue lobe of the millimeter SiO jet peaks 10 au away from the star (Fig. 4) with no evidence of central emission associated with the disk. The non-detection of millimeter SiO on-source implies an infrared SiO emitting radius of <2.2 au, consistent with the 1-1.2 au radius from the infrared line widths (see Methods).

2 Discussion

In chemical equilibrium from solar composition gas (Mg/Si=1.07), [2, 28], refractory solids condense sequentially, beginning with calcium- and aluminum-rich minerals between 1650 and 1300 K and continuing between 1320 and 300 K with the condensation of the minerals forsterite and enstatite, with $N_{enstatite}/N_{forsterite}$=0.5-0.8 below 1000 K [29]. This sequence and gas-grain reactions exhaust the gaseous SiO, with insufficient leftovers to condense silica [29–31]. Certain meteorites contain millimeter-sized agglomerates of such minerals in the form of calcium- and aluminum-rich inclusions (CAIs) and amoeboid olivine aggregates (AOAs), some of which have fine-grained (micron-sized) textures and enhanced ^{16}O isotopic signatures indicative of co-spatial condensation in the innermost Solar Nebula [32, 33]. However, the crystalline silicates observed in protoplanetary disks [34, 35] are attributed to amorphous interstellar silicates that *either* annealed below 1300 K or vaporized above 1300 K and re-condensed as crystals. If HOPS-315's forsterite and enstatite are associated with AOAs formed by sublimation and re-condensation, then their detection implies prior condensation of CAIs.

Several signs point to a *vertical* condensation origin for HOPS-315's crystalline silicates. Beyond 0.5 au, protostellar disk models predict annealing timescales longer than the typical Class I lifetime of 0.1 Myr [14]. Additionally, the presence of 472 K SiO gas implies (partial) silicate vaporization at $T \geq$1300 K (from which SiO, Si^0, Mg^0, and Fe^0 are the main products [24]), with subsequent cooling, which must be accompanied by condensation. Vertical mass flows near the water snowline are seen to advect vapor from the warm midplane to the cool temperature inversion layer, where it re-condenses, in hydrodynamical simulations of optically thick disks dominated by viscous heating [36]. An analogous mechanism at the outer edge of the thermostat region at 1 au, combined with the increased turbulence there [37], could mix

freshly sublimated SiO from the midplane into the disk atmosphere, condensing CAIs near the disk midplane and AOAs in the cooler temperature inversion layer above, explaining HOPS-315's SiO column density, blue-shifted velocity, and the observed crystals (Figure 1). Whether this flow contributes to the base of the disk wind is an interesting question that could be important for understanding the outward radial transport of CAIs and AOAs by winds or viscous evolution, which are predicted to seed these solids into the comet-forming regions of disks [38–40].

The association of these crystals with AOA-analogs is strengthened by HOPS-315's lack of strong Mg^0 and Fe^+ emission, despite a high SiO column density, which suggests the condensing gas reservoir has a low gaseous Mg/Si ratio. This would naturally result if as little as 0.47% of the condensates became chemically isolated from the SiO reservoir, e.g. by the aggregation of sub-micron forsterite into micron-sized agglomerates analogous to AOAs [28, 31]. This decreases the efficiency of gas-grain reactions, forcing the expenditure of both Mg and SiO through enhanced enstatite condensation until the vapor Mg/Si ratio drops below unity, allowing small amounts of silica to condense from the excess SiO gas [28, 29]. Condensation under solar values of Mg/Si is ruled out at a $>3\sigma$ level by HOPS-315's high $N_{enstatite}/N_{forsterite}$ of $2.8^{+5.8}_{-1.2}$, and the tentative detection of silica is consistent with this scenario. Aggregates larger than 10 μm have a gray opacity through the 10 μm feature and would not be detectable [e.g. Figure 3a of 12].

Partial isolation condensation models can reproduce textures and compositions of meteoritic AOAs with 5 μm forsterite grains and silica inclusions, provided gas pressures larger than $P = 10^{-5}$ bar and vapor depletion of H and He by a factor of 10 (effectively an increase in the solids-to-gas ratio of the feedstock material, [31]). Midplane pressures of the thermostat region in highly accreting disks reach $P > 10^{-5}$ bar [12], sufficient to isolate forsterite. Gravitational dust settling and inward dust motion increase the midplane solids-to-gas ratio over the interstellar value by up to a factor of 400 in the inner 1-10 au of protostellar systems [41].

A high midplane dust/gas ratio could yield a high SiO/CO ratio in the gas accreting onto the star or launching into the jet. However, the millimeter $N_{\rm SiO}/N_{\rm 12CO}$ ratio in HOPS-315's jet suggests 98.3% of the expected silicon is missing (Methods). A dust-rich jet could explain such gas depletion, but our earlier arguments suggest the jet and wind are dust-poor. Additionally, the CO overtone band may probe the base of the vertically extended jet at 0.54 au at 3754^{+46}_{-44} K (see Extended Data Table 2). Since the SiO overtone band at 4μm, which samples comparable temperatures, is not detected, the SiO gas may not extend towards the star. Therefore it seems more likely that solids are sequestered outside of the edge of the thermostat region.

SiO-rich solids could be preferentially retained relative to C-rich solids either through pebble trapping or planetesimal formation anywhere between the water snowline and the outer edge of the thermostat region, where silicates vaporize [42]. The water ice snowline is the location favored by the meteoritic record for the earliest generation of

planetesimal formation, due to signatures of hypervolatiles and oxidized iron in the known meteorite populations [43, 44]. However, it is still an open question whether the solar system meteoritic record is complete, or whether the early formation of planetesimals near the thermostat region could be possible in other protoplanetary systems (see discussion in [44]).

HOPS-315 shows signatures of refractory solids that likely re-condensed from a high-pressure gaseous reservoir of sublimated interstellar silicates, similar to the formation conditions of AOAs and CAIs in the early Solar System. The average Class I protostellar age of 0.135±0.011 Myr (Methods) is comparable to the CAI and AOA production timescale of 0.160 Myr [3]; despite its unusual spectrum, HOPS-315 may represent a common protostellar evolutionary stage caught at the ideal orientation and moment of time to show these features [38]. The clear evidence for re-condensation of silicates vaporized in a disk thermostat region favors this region's role in the formation of CAIs [14], while the low Si/C abundance in the jet suggests that conditions are ripe for planet formation, or it may already have begun. Since the Solar System's first planetesimals, iron-meteorite parent bodies, coalesced 0.1−0.3 Myr after CAI formation [45, 46], HOPS-315 represents a unique opportunity to study the physical and chemical conditions during the earliest stages of planet formation, previously accessible only through the Solar System's meteoritic record.

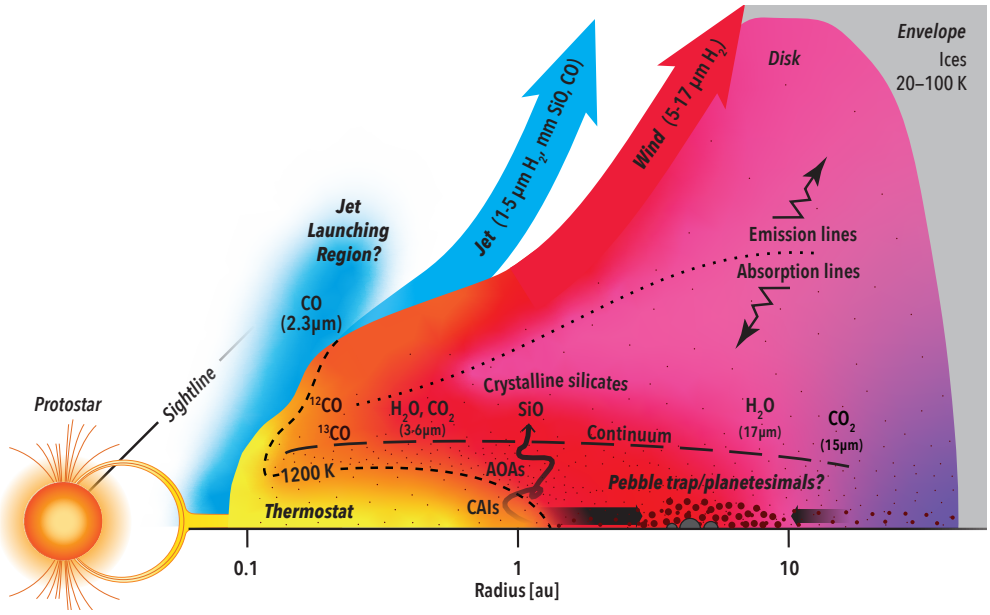

Fig. 1 Structure of HOPS-315's inner disk. Molecules located above the temperature minimum (dotted line) are seen in emission. Molecules located between the temperature minimum and the disk photosphere (long-dashed line) are seen in absorption. Dust sublimates in the thermostat region near 1 au (short-dashed line), releasing SiO. Turbulent transport there leads to vertical condensation of CAIs and AOAs, of which the co-spatial SiO and crystalline silicates are remnants.

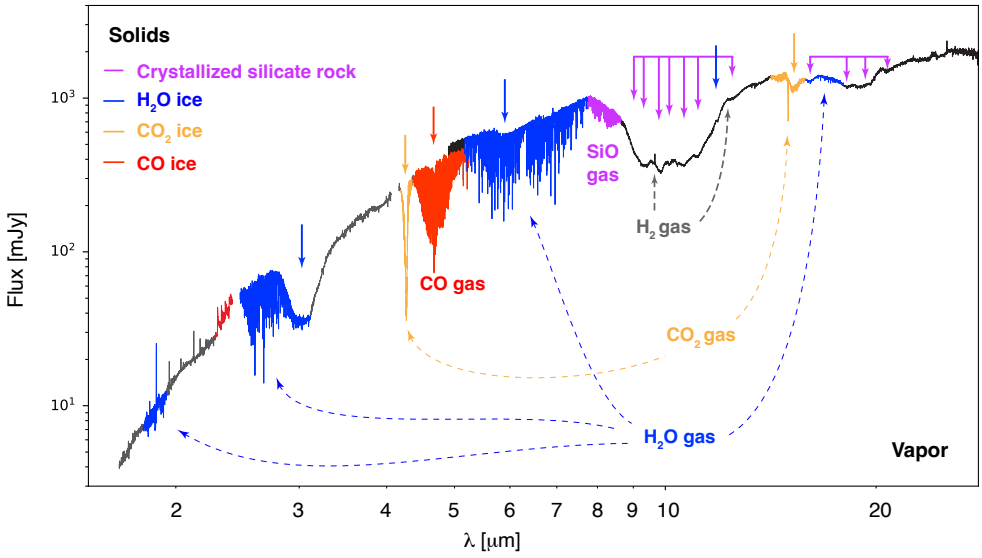

Fig. 2 JWST spectrum of HOPS-315. (A) Bands of ice and thermally processed silicates are seen, along with (B) molecular gas absorption bands and (select) H_2 emission lines probing different temperatures and densities. Warm SiO gas probes vaporized rocks, while crystalline silicates may probe condensed SiO gas.

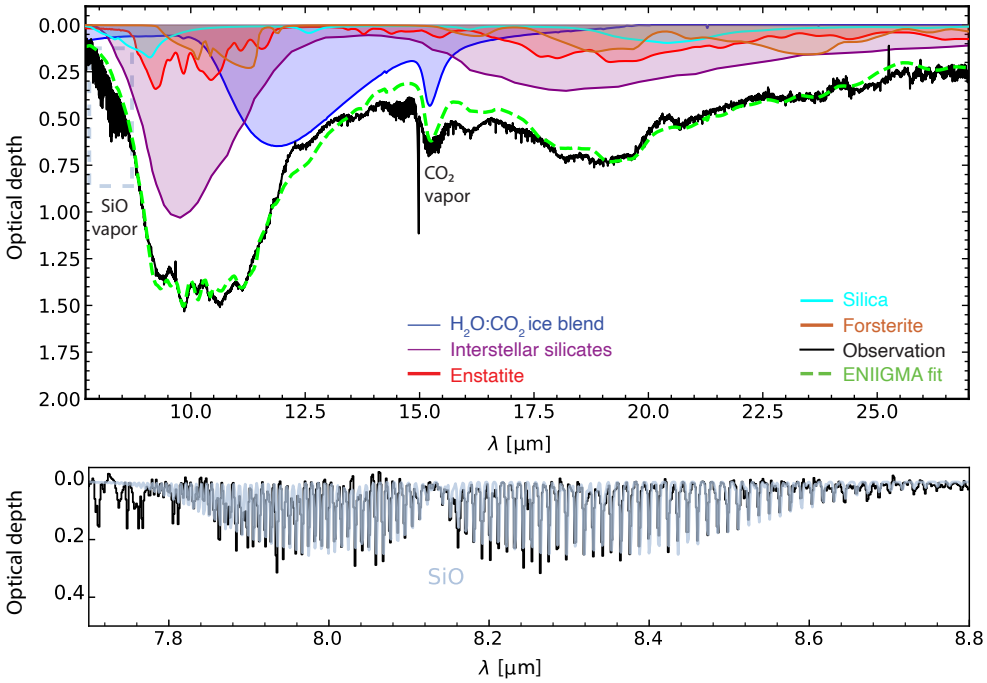

Fig. 3 JWST crystalline silicate and SiO vapor analysis. *Top panel:* Plot of the statistically significant components found by our `ENIIGMA` fit of laboratory mass absorption coefficients for CAI and AOA minerals. Below 18 μm, bands of 'noise' are the molecular vapor absorptions labeled in Fig. 2. The blue box indicates the SiO gas modeled below. *Bottom panel:* Slab model fit to the SiO vapor band (ν=1-0 Σ-Σ) at 8.05 μm.

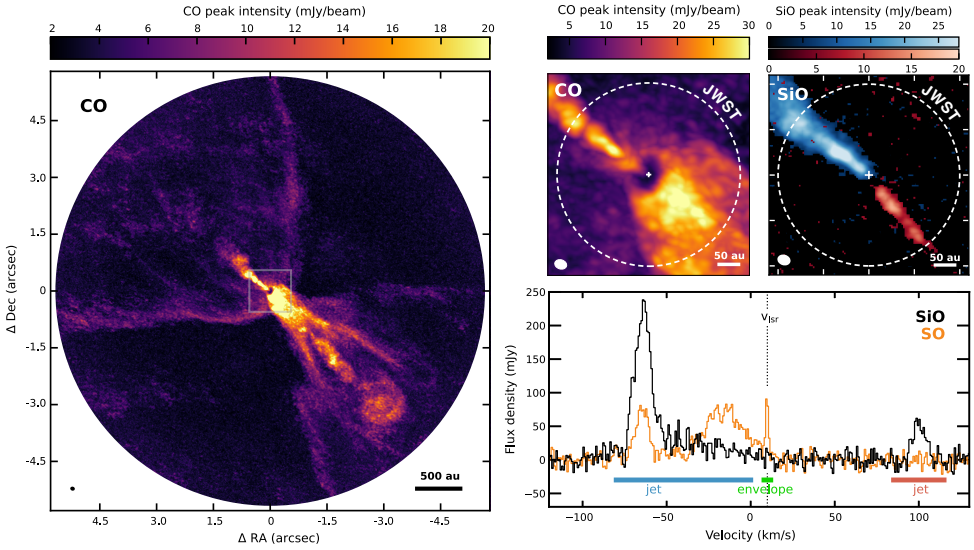

Fig. 4 ALMA maps and spectra of HOPS-315.(Left) ALMA CO map showing the wide-angle outflow and molecular jet. (Middle, top) Zoom on the central region, revealing the direct inner disk sightline, indicated by the positioning of the jet relative to the stellar location (cross) in front of the shadow caused by the optically thick dust continuum. (Right, top) ALMA SiO map showing the non-detection of millimeter SiO emission in the disk. (Right, bottom) SiO and SO spectra in the LSRK velocity reference frame confirm that there is no contribution to the millimeter SiO from a disk wind or gas at the source velocity. Circle is representative JWST extraction aperture.

3 Methods

3.1 System properties

The isolated single Class I protostar HOPS-315 is still embedded in a dusty protostellar envelope with a $i = 40° \pm 8$ inclination [25] that provides a sightline down the outflow cavity wall to the hot gas accreting from the disk onto the star at A_K ∼4.1 magnitudes of extinction [5]. The central K7 protostar has a mass of 0.6 $M_\odot$, with an accretion luminosity L_{acc}=3.2 $L_\odot$ and stellar luminosity L_{star}=3.7 $L_\odot$, and a mass accretion rate of $\dot{M} \sim 8.5 \times 10^{-7}$ $M_\odot$ yr^{-1} [5]. With this accretion rate, HOPS-315 should become a solar mass pre-main sequence star by 1 Myr.

The average age for a Class I protostar is 0.135±0.011 Myr, equal to the sum of the half-lives of the Class 0 (0.047±0.004 Myr) and Class I (0.088±0.007 Myr) stages [6], which is bootstrapped from population statistics and older systems with known ages. The detection of millimeter SiO in HOPS-315's jet is more consistent with a Class 0 age [25]. [47] measure an 870μm disk dust mass of M_{dust}=105.6±2.0 $M_\oplus$ (or ∼0.03 $M_\odot$, assuming a gas/dust ratio of 100), making HOPS-315's disk more massive than 80% of Orion Class I's, and essentially average for a Class 0. However, their disk radius of R_{disk}=45.6±10.0 AU is average for a Class I and smaller than 60% of Class 0 disks, suggesting that HOPS-315's disk is particularly dense and likely on the younger end of the Class I evolutionary stage.

Based on SiO knots in its jet, HOPS-315 has outbursting events on a ∼50 year timeframe [25]. The infrared lightcurve has only recently begun rising after remaining flat for two decades, but the crystalline silicate absorption features in the MIRI spectrum cannot be associated with this outburst, as they were equally strong in two *Spitzer* IRS spectra taken in 2005, 18 years before our observations. This argues in favor of their origin in a non-transient disk structure, like the midplane thermostat region.

3.2 Observations and data reduction.

JWST: HOPS-315 was observed by JWST with MIRI Medium Resolution Spectroscopy (MRS) on March 15th, 2023, through program 1854 (PI M. K. McClure). We used a standard 4-point dither pattern centered on the IRAC coordinates, with target acquisition to center the source. The total science exposure was 222 seconds using the FASTR1 readout pattern. The data were processed through JWST pipeline version 1.12.3 [48], which includes the time-dependent correction for the throughput of channel 4. The calibration reference file database versions 11.16.21 and *jwst_1141.pmap* was used, which includes updated onboard flat-field and throughput calibrations for an absolute flux calibration accuracy estimate of 5.6 ± 0.7% [49]. We performed the standard steps in the JWST pipeline to process the data from the 3D ramp format to the cosmic ray corrected slope image. A dedicated sky observation taken nearby was used to subtract the astrophysical background from the target's flux after the "Level 1" run, while additional processing of the 2D slope image for assigning pixels

to coordinates, flat fielding, and flux calibration was also conducted using standard steps in the "Level 2" data pipeline calwebb_spec2. We ran the "Stage 3" pipeline to build the calibrated 2D IFU slice images in the 3D datacube. The 3D cube of the final pipeline processed product was built with the outlier bad pixel rejection step turned off, as it over-corrected pixels and removed target flux.

The JWST-NIRSpec/IFU observations were taken on September 15th, 2023, using the G235H and G395H filters. We used a 4-point cycling dither pattern, starting from position 6. The integration time was 233 seconds with an NRSIRS2RAPID readout pattern. We did not take a background frame, but because HOPS-315 resides in a region with bright backgrounds, we corrected for stray light in the failed open MSA shutters by taking a leakcal observation at each dither position. We used the standard 3D cube taken from the MAST archive using the calibration reference file database versions 11.17.2 and *jwst_1130.pmap*.

For both MIRI and NIRSpec, the spectrum in each subchannel was extracted using a conical extraction with a circular aperture whose radius was 2.5× the resolution element at each wavelength, with a minimum radius of 1.25 arcseconds.

ALMA: HOPS-315 was observed with ALMA located on Ilano de Chajnantor in Northern Chile on November 19, 2023. The observations were conducted in three consecutive executions with a maximum baseline length of 6582 m for a total on-source time of roughly 106 minutes. The monitored quasar J0423–0120 was the bandpass and absolute flux calibrator in the first and second execution, and J0538–4405 was the bandpass and flux calibrator during the third execution. The phase calibrator was J0527+0331 in all executions. The central frequency of the observations was roughly 344.8 GHz (Band 7), covering the CO $J = 3 - 2$ (345.795990 GHz), SiO ν=0, $J = 8 - 7$ (347.330579 GHz) and SO $8_8 - 7_7$ (344.310612 GHz) transitions. The absolute flux density uncertainty in Band 7 is expected to be roughly 5%.

The data were reduced and imaged using the ALMA calibration pipeline version 2023.1.0.124 within CASA v.6.5.4.9 [50]. This included self-calibration on the continuum data after which the phase and amplitude solutions were applied to the line data, and continuum subtraction based on a fit to the line-free continuum regions in uv-space. The molecular lines were imaged using a robust parameter of 0.5 (resulting in a beam size of $0.06'' \times 0.05''$), an image size of 2250×2250 and a pixel size of $0.0095''$. A channel spacing of 0.4 km s^{-1} was used for SiO, and 0.85 km s^{-1} for CO and SO. A primary beam correction was applied to all images. The rms per channel is roughly 1.4 mJy beam^{-1} for SiO, 1.0 mJy beam^{-1} for CO and 0.92 mJy beam^{-1} for SO. The maximum resolvable scale (MRS) is $0.8''$. We measure a local system velocity of $v_{\rm system}$=9.68 ±0.19 km s^{-1} in the LSRK velocity reference frame by fitting a Gaussian to the narrow, central SO component. This value is consistent with the $v_{\rm system}$=9.9 km s^{-1} found by [25] using their peak C^{18}O emission with 1.4 km s^{-1} resolution.

The size of the infrared SiO emitting region can be constrained from the ALMA non-detection of SiO at the stellar position. Based on the column density derived from the JWST SiO absorption, the observed millimeter transition should be optically thick. A reservoir of SiO at the measured temperature of 488 K with a radius of 10 au (half the ALMA beam) should have been easily detected, both in the millimeter SiO image and with a narrow central component, similar to that seen in our SO spectrum and the $C^{18}O$ from [25]. The rms in the SiO image is 6.34 K per channel at the native velocity resolution of 0.4 km s^{-1}, so the JWST SiO should arise within an circular area with a radius of 2.2 au to not be detected in the ALMA observations, assuming a 3σ noise limit. If the emitting area of the infrared SiO is an annulus rather than a circular area, the area would be equivalent to a circle with 2.2 au radius.

We calculated CO and SiO column densities from the integrated flux extracted in a $0.2''$ radius aperture centered $0.32''$ off-source along the jet, within the spectral velocity range of the blueshifted SiO jet (-75.6 – -50.7 km/s). The aperture was chosen to match the brightest knot in the H_2 1-0 S(1) jet emission found by [18]. We assumed gas at 150 K, following Section 3.3 of [25], with molecular line parameters from the Cologne Database for Molecular Spectroscopy [51].

3.3 Solid state fitting

HOPS-315's JWST spectrum encompasses numerous solid-state absorption features (Fig. 2), including ices and amorphous silicates, which may arise in both the protostellar envelope and young disk. The three bands of H_2O ice at 3, 6, and 12 μm trace temperatures T <130 K. Two CO_2 ice features appear at 4.27 and 15.3 μm; the profile of the latter is consistent with CO_2 ice trapped in an H_2O ice matrix [52], rather than pure CO_2 ice, suggesting temperatures between the CO_2 sublimation temperature of T=70 K and the H_2O crystallization temperature around 130 K. The CO ice absorption at 4.7 μm traces material at T <20K. Superimposed on the broad amorphous silicate features from 8-10 μm and 16-21 μm, we see sharp absorption features indicative of crystalline silicates, which can only be produced in the hot inner regions of the young disk above ∼800 K. To identify the minerals with the most statistically significant contribution to these sharp features, we analyze the 5-28 μm region.

To isolate the crystalline silicate features, we first fit a fourth order polynomial to the regions indicated in the figure, fitting slightly above the data continuum in order to leave room for the optical depth spectra, which have some non-zero baseline absorption. This continuum was used to calculate the optical depth, $\tau = -ln(F_{spectrum}/F_{continuum})$. This step has a large systemic uncertainty that is influenced by the source geometry and temperature gradient giving rise to the strong continuum. Extensive radiative transfer modeling, beyond the scope of this work, is required to fully account for the systematic uncertainty on the optical depth spectrum.

For the ice and minerals listed in Extended Data Table 1, we calculated opacities from laboratory refractive indices using the OPTOOL software package [53] to correct

for grain shape and size effects with a continuous distribution of ellipsoids (CDE) of size distribution $n(a) = n_0\ a^{-3.5}$, with 0.005 μm $\leq a \leq a_{max}$. For the ice mixture, the $a_{max} = 1$ μm, while for the refractory minerals, we assumed $a_{max} = 0.25$ μm, as direct condensates initially form smaller grains, and such grains produce sharper features than larger grains. The temperatures of the laboratory refractory minerals were between 273 and 300 K; higher temperatures shift the peak wavelength positions, but temperature dependent data sets were only available for a small subset of the tested minerals. The refractive index for the ice was calculated from an absorbance spectrum of H_2O:CO_2 (10:1) ice mixture at 130 K from [52], using the `NKABS` code [54], an ice thickness of 0.5 μm, and $n_0 = 1.32$. The latter accounts for the refractive profile below 2 μm, where the laboratory data begins. The 10:1 mixture was the only binary mixture of these ice species presently available in the Leiden Ice Database for Astrochemistry (LIDA) [54]; there were no other strong ice components present in this part of the MIRI spectrum. For each mineral, we calculated the optical depth spectrum from the opacities. For minerals with multiple polymorphs, e.g. silica and enstatite, we considered only the most common polymorphs found in protoplanetary disks by previous authors [34, 35]. To represent interstellar silicates, we used the Galactic Center Source (GCS3) template [55].

We performed `ENIIGMA` fits on the MIRI range of HOPS-315, between 7.7 and 27.7 μm, where the strong silicate features are visible. The `ENIIGMA` methodology, described fully in [56], uses genetic modeling algorithms to find the global minimum fit from a linear combination of the infrared optical depth spectra calculated from the opacities described above. We performed fits with the ice blend, interstellar silicates, and all of the refractory mineral components; however, our results showed that only the five minerals discussed in the main text were statistically significant. We refer to this model as 'M5(w)' in Extended Data Table 1. We also calculated the confidence intervals on the abundance of each mineral with `ENIIGMA`, with the 3σ confidence level reported in Extended Data Table 1 and corner plot reported in the Supplementary Information (Supplementary Methods Figure 1). The 3σ confidence intervals are never below 0, which indicates that all of the listed minerals improve the fit.
However, the quality of the silica and forsterite fits is impacted by the slope of the continuum fit from 11-15 μm, under the 12.5 μm crystalline silica feature. This continuum could be impacted by a temperature gradient in the H_2O:CO_2 ice mixture, which would shift the ice's peak from 11.8 μm either shorter or longer wavelengths; this would impact the fit to the 12.5 μm silica feature and the 11.3 μm forsterite feature. Exploring the presence of temperature gradients requires a different modeling setup that will be explored in a future work.

To explore the systematic uncertainty in the silica abundance, we produced a second fit between 7.75 and 28 μm without silica, as shown in Extended Data Figure 2. This 4-component, wide model ('M4(w)') reproduces the 20 μm features marginally better than our standard model, but is a poorer match to the 8-9.5 and 11.5-13 μm slopes. A quality assessment using the reduced chi-squared (χ^2_r) and Akaike Information Criterion (AIC) metrics, as described in the Supplementary Information, indicates that

over the 7.75-28μm range, the M5(w) model with silica provides a better fit than the M4(w) model without silica by the χ^2_r metric (χ^2_r=7.28 versus 8.13, respectively) but not by a statistically significant amount according to the AIC metric (AIC=17.29 versus 16.14, respectively), since the difference in AIC is less than 2 [57].
Since the 10 and 20 μm silicate complexes trace different radial locations when seen in emission [11, 34, 35], we tested whether the silica model might be robust when limiting the fits to the three silica features at 8.2, 9.0, and 12.5 μm with a shorter wavelength range from 7.75-13.2 μm, as shown in Extended Data Figure 3. For the shorter wavelengths, the model with silica, M5(s), is statistically preferred over the model without silica, M4(s), with both metrics, as χ^2_r=6.71 versus 14.37 and AIC=16.72 versus 22.37, with ΔAIC>2. Specifically, the absorption from 8-9 μm is improved, along with the shape of the absorption at 12.5μm. Therefore we conclude that crystalline silica is (tentatively) present in the 10 μm complex, given our modeling approach and the laboratory data to which we have access, on the basis of the statistically better fit to the 8-9 μm and 12-13 μm absorption. Future modeling that includes temperature gradients in the silicates and ices and tests to rule out additional, less common, polymorphs of enstatite and silica would confirm this silica detection.

3.4 Slab model fitting

To analyze the molecular features, we adopt the local thermodynamic equilibrium (LTE) slab models of [58], adapted from the LTE emission models of [59, 60]. These models assume that the line absorption comes from a region with a single temperature and density, whereas disks have gradients in both parameters. However, comparison between slab models and full, 2D chemical models of the same disk [26, 61] shows that, for a given molecular band, the slab model closely approximates the mean temperature and density of that band's emitting area in the 2D model, although it may not recover values at either extreme of the gradient. To compensate for this effect, we fit each molecular band of each species individually, as they likely trace different disk regions.

Our models use molecular spectroscopy data from the LAMDA and HITRAN databases to compute the level populations, assuming they are in LTE with a single excitation temperature $T_{\rm ex}$. The partition functions needed for the model calculations are taken from the TIPS database. The LTE assumption should be robust for the dense, collisionally-dominated disk environment. We compute the line center optical depth of each transition assuming a single column density, N, and line width, ΔV, following [60]. A synthetic optical depth spectrum is created by sampling the lines at high resolution ($R = 10^6$), assuming a Gaussian line profile of full-width at half-maximum ΔV. For the absorption features, we immediately convolve with the instrument response.

For the CO overtone emission feature, we correct the emission for extinction assuming A_V=38 from [17] using the extinction curve of [62], and then convert the optical depth spectrum $\tau(\lambda)$ to flux units via $F(\lambda) = \pi \left(\frac{R}{d}\right)^2 B_\nu(T_{\rm ex})(1 - e^{-\tau(\lambda)})$, where R is

the characteristic radius of the emitting slab, $d = 420$ pc is the distance to the source, B_ν is the Planck function, and τ is the line optical depth. We caution that the characteristic radius R is simply a scaling factor for the emitting area of the cylindrical slab which is assumed to represent the emission, and should not be interpreted as a disk radius without constraints on the geometry of the emitting region.

To fit the observed molecular absorption features, we fit a baseline to the observed spectrum using a guided cubic spline and convert from flux to optical depth units via $\tau_{\rm obs} = -log(F_{\rm obs}/F_{\rm baseline})$. Although JWST cannot velocity-resolve these lines, our high SNR constrains ΔV through the amplitude and line profile shapes in cases where the absorption lines have sufficient optical depth. Similarly, we can constrain large velocity shifts of the molecular bands, finding good agreement assuming rest frame wavelengths in the barycentric system, or blueshifted by 20-30 km s^{-1} with respect to the ALMA source velocity of +9.68 km s^{-1} in the LSRK velocity frame. To determine the best fit values for each band, we use a Bayesian analysis where the likelihood assumes the observed optical depth to have a Gaussian noise of 0.01 τ and a uniform prior over the model parameters: N, ΔV, and $T_{\rm ex}$. In this case, the likelihood function is $\frac{1}{2}\chi^2$, and finding the best-fit model is effectively a χ^2 minimization. We use the Markov chain Monte Carlo sampling method from the python package `emcee` [63] to sample the posterior probability. Corner plots for all modeled bands are given in Supplementary Methods Figures 2-12.

We calculated the disk radii at which each band absorbs from the ΔV, assuming that the line width is Doppler broadened, $\Delta V = v_{Doppler}\ sin(i)$, using i=40°. We consider that $v_{Doppler}$ is mostly due to Keplerian motion of the disk, $v_{Keplerian} = \sqrt{(GM_* R_{disk}^2)/(R_{disk}^2 + z_{disk}^2)^{3/2}}$. Extended Data Table 2 reports a range of radii for two limiting cases: one where z_{disk}/R_{disk}=0.2, which is the approximate vertical height of the disk photosphere in [14], and the other z_{disk}/R_{disk}=0, at the disk midplane, which provides an outer limit despite being unphysical given the optical depth of the inner disk. Increasing the absorption height pushes the radius closer to the star. Turbulent contributions to the line width would push the radii farther out in the disk. Typical values for turbulence in the inner disk range from 7-15 km s^{-1} in hot, ∼1500 K H_2O and CO overtone emission [64], but our temperatures are substantially less than that for all absorption bands.

To determine whether the SiO absorption originates in the jet, we fit a Gaussian profile to bright and well resolved $\nu = 1 - 0$ transitions of SiO between 7.9 and 8.5 μm and compute the velocity offset from the barycentric rest-frame wavelength of each transition, the results of which are shown in Extended Data Figure 1. The mean velocity offset is 6.7 ± 1.2 km^{-1}, with the uncertainty calculated from the standard error in the mean of σ/N, with N the number of lines fit. Converting to the LSRK reference frame, this is -10.6±1.2 km s^{-1}, consistent with an infrared SiO origin in the disk rather than in the high-velocity jet.

Aside from H_2, the only detected molecular emission is the CO overtone band at 2.3 μm, which we similarly fit with a Bayseian method. However, the emitting radius R is an additional parameter, and ΔV is fixed to the best-fit value of the ^{12}CO absorption of 37.7 km s^{-1}, necessitated by severe line blending in the bandhead. This value is physically motivated if the overtone emission probes the outflowing CO launched from the inner edge of the thermostat region.

H_2O: Four bands of gaseous H_2O are present in these spectra, three of which are fit in Extended Data Figure 4. The ro-vibrational water bands at 2.5–3 μm and 5–6 μm and the rotational water at 15–17 μm all trace a reservoir of warm gas between 400–525 K and column densities of 10^{18}–10^{19} cm^{-2}. The two colder bands trace higher column densities between 0.3−0.6 AU of the star. In contrast, the hotter band traces less dense material nearly 11 AU away but closer to the disk photosphere, based on its weaker optical depths.

C_2H_2 and HCN: The absorption bands of C_2H_2 and HCN gas both probe warm gas near 0.1 AU from the star at temperatures between 500-700 K but at columns of 10^{15}–10^{16} cm^{-2}, shown in Extended Data Figure 5. Despite the excellent SNR of these data, there are large uncertainties on the C_2H_2 fit in particular, due to the weakness of the features. Their weak optical depth indicates that these molecules likely originate near the disk photosphere, consistent with their predicted location from 2D disk chemical models for emission spectra [26].

CO_2: The 4.27 μm gas absorption traces higher temperatures and lower column densities than the 15.3 μm band, 351 K and 10^{17} cm^{-2} at 0.40 au versus 124 K and 10^{19} cm^{-2} at 18.11 au, respectively (Extended Data Figure 6), opposite to the pattern seen for water. This may indicate that more of the carbon budget is carried by the CO_2 gas at 18 au, sublimated from the H_2O:CO_2 ice, while a larger fraction of the gaseous carbon at 0.40 au may be carried by CO.

CO: the CO fundamental gas band shows multiple absorption components (Extended Data Figure 7). We fit the unblended ^{13}CO component and a single ^{12}CO component at 646 K and 9.14×10^{17} cm^{-2} and 1181 K and 7.39×10^{18} cm^{-2}, respectively. The temperature of the ^{12}CO is consistent with gas at the upper, low density end of the silicate sublimation front in mature protoplanetary disks [12], consistent with the radius of 0.16±0.01 au implied by its best-fitting ΔV value. Converting the ^{13}CO column, located at 0.17±0.02 au, to ^{12}CO, assuming the interstellar ratio [65], yields a column of 6.30×10^{19} cm^{-2}, confirming that these CO components probe downward through vertical structure in the temperature inversion layer at similar radii.

However our fits also demonstrate the presence of additional, optically thick temperature components, both a warm ^{12}CO not found by our models and, in the residuals of this fit, a missing cold ^{12}CO component, $T \leq$40 K, that may correspond to the disk wind seen in ALMA ^{12}CO emission or the protostellar hot core [66] (see Extended Data Figure 7 and Supplementary Methods Figure 11). However, the high optical

depth of the cold CO lines is difficult to reconcile with the observations without a very large ΔV that is ruled out by the line profiles. This suggests that the covering fraction of the continuum against which the hot and cold components are absorbing may be spatially different due to the geometry of the system, and therefore the optical depth of the cold component may be lower than we derive using the current continuum. Higher temperature outflowing material may potentially contribute to the CO overtone emission at 2.3 μm; the best-fitting emitting radius of 0.54 au, high temperature of 3775 K, and high density of 2.40×10^{21} cm^{-2} suggest that it traces not only the superheated disk atmosphere above the inversion layer but also the same outflowing material probed by the H_2 emission seen by [18]. However, since the CO gas and outflow structure is not the scientific focus of this paper, we leave a more complex model of the different components to a future work.

3.5 Disk silicate retention calculation

The column densities of CO and SiO in the jet are $N_{\rm CO,jet}=1.52\times10^{17}$ cm^{-2} and $N_{\rm SiO,jet}=2.78\times10^{14}$ cm^{-2}, respectively, leading to $({\rm Si/C})_{\rm jet}=2.4\times10^{-3}$, or only 1.7% of the expected Si, assuming cosmic Si/C. Since the jet abundances should reflect the abundance at the jet launching radius in the disk, which is just interior to the silicate sublimation radius, the jet's silicon depletion suggests that 98.3% of the silicon is being retained in the disk as condensed silicates, while the carbon is fully launched into the jet as CO gas.

Supplementary information. We have supplementary information in a separate file.

Acknowledgments. This work is based in part on observations made with the NASAESACSA James Webb Space Telescope. The data were obtained from the Mikulski Archive for Space Telescopes at the Space Telescope Science Institute, which is operated by the Association of Universities for Research in Astronomy, Inc., under NASA contract NAS 5-03127 for JWST. These observations are associated with program #1854. This paper makes use of the following ALMA data: ADSJAO.ALMA#2023.A.00009.S. ALMA is a partnership of ESO (representing its member states), NSF (USA) and NINS (Japan), together with NRC (Canada), MOST and ASIAA (Taiwan), and KASI (Republic of Korea), in cooperation with the Republic of Chile. The Joint ALMA Observatory is operated by ESO, auI/NRAO and NAOJ. The National Radio Astronomy Observatory is a facility of the National Science Foundation operated under cooperative agreement by Associated Universities, Inc.

E.v.D, L.F., and W.R acknowledge funding support from the European Research Council (ERC) under the European Union's Horizon 2020 research and innovation programme (grant agreement No. 101019751 MOLDISK), from the TOP-1 Dutch Research Council (NWO) grant 614.001.751 and from the Danish National Research Foundation through the Center of Excellence "InterCat" (Grant agreement no.: DNRF150). E.A.B. acknowledges support from NASA XRP #80NSSC24K0149. E.D. and J.A.N. acknowledge support from French Programme National 'Physique et Chimie du Milieu Interstellaire' (PCMI) of the CNRS/INSU with the INC/INP, cofunded by the CEA and the CNES. D.H. is supported by a Center for Informatics and Computation in Astronomy (CICA) grant and grant number 110J0353I9 from the Ministry of Education of Taiwan. D.H. also acknowledges support from the National Science and Technology Council, Taiwan (Grant NSTC111-2112-M-007-014-MY3, NSTC113-2639-M-A49-002-ASP, and NSTC113-2112-M-007-027).

- Availability of data and materials: The original data is publicly available through the JWST MAST archive and ALMA archives. Our version of the 1D extracted spectra are on Zenodo at URL (update once publication date is clear).
- Code availability: The solid state fitting code ENIIGMA developed by W.R. is publicly available on GitHub: https://github.com/willastro/ENIIGMA-fitting-tool. The slab model used in this work is a private code developed by L.F. and collaborators, based on the private code developed by Benoit Tabone for emission line slab models. It is available from L.F. upon request.
- Authors' contributions: MKM, MvtH, EB, DH, EvD, JAN, DQ, and ED contributed to the JWST proposal. MvH, EB, and MKM contributed to the ALMA proposal. MKM, JAS, and MvH reduced the JWST NIRSpec/MIRI and ALMA data, respectively. MKM, MvtH, EB, LF, and WR designed the analysis plan. LF and WRMR designed and executed the JWST gas and solids modeling, with ancillary analysis by MKM and input from EvD. MvtH and EB designed and executed the ALMA analysis. JHB provided re-formatted molecular data for the SiO band. MKM wrote the

majority of the main text. MvtH, LF, WRMR, and MKM wrote parts of the Methods section. All authors participated in discussion of the observations, interpretation of the results, and commented on the submitted draft.

References

[1] McDonough, W. F. & Sun, S. s. The composition of the Earth. *Chemical Geology* **120**, 223–253 (1995).

[2] Lodders, K. Solar System Abundances and Condensation Temperatures of the Elements. *The Astrophysical Journal* **591**, 1220–1247 (2003). URL https://ui.adsabs.harvard.edu/abs/2003ApJ...591.1220L. Publisher: IOP ADS Bibcode: 2003ApJ...591.1220L.

[3] Connelly, J. N. *et al.* The Absolute Chronology and Thermal Processing of Solids in the Solar Protoplanetary Disk. *Science* **338**, 651–655 (2012). URL https://www.science.org/doi/10.1126/science.1226919. Publisher: American Association for the Advancement of Science.

[4] Lichtenberg, T., Schaefer, L. K., Nakajima, M. & Fischer, R. A. Geophysical Evolution During Rocky Planet Formation **534**, 907 (2023). URL https://ui.adsabs.harvard.edu/abs/2023ASPC..534..907L. Conference Name: Protostars and Planets VII Place: eprint: arXiv:2203.10023 ADS Bibcode: 2023ASPC..534..907L.

[5] Antoniucci, S., Nisini, B., Giannini, T. & Lorenzetti, D. Accretion and ejection properties of embedded protostars: the case of HH26, HH34, and HH46 IRS. *Astronomy & Astrophysics* **479**, 503–514 (2008). URL https://www.aanda.org/articles/aa/abs/2008/08/aa7468-07/aa7468-07.html. Number: 2 Publisher: EDP Sciences.

[6] Kristensen, L. E. & Dunham, M. M. Protostellar half-life: new methodology and estimates. *Astronomy and Astrophysics* **618**, A158 (2018). URL https://ui.adsabs.harvard.edu/abs/2018A&A...618A.158K. ADS Bibcode: 2018A&A...618A.158K.

[7] Sperling, T. *et al.* Probing the hidden atomic gas in Class I jets with SOFIA. *Astronomy & Astrophysics* **642**, A216 (2020). URL https://www.aanda.org/articles/aa/abs/2020/10/aa37242-19/aa37242-19.html. Publisher: EDP Sciences.

[8] Carr, J. S. Infrared CO Emission and Disks around Young Stars. *Astrophysics and Space Science* **224**, 25–28 (1995). URL https://ui.adsabs.harvard.edu/abs/1995Ap&SS.224...25C. Publisher: Springer ADS Bibcode: 1995Ap&SS.224...25C.

[9] Najita, J. R., Doppmann, G. W., Carr, J. S., Graham, J. R. & Eisner, J. A. High-Resolution K-Band Spectroscopy of MWC 480 and V1331 Cyg. *The Astrophysical Journal* **691**, 738–748 (2009). URL https://ui.adsabs.harvard.edu/abs/2009ApJ...691..738N. Publisher: IOP ADS Bibcode: 2009ApJ...691..738N.

[10] Lyo, A. R. *et al.* Inner Warm Disk of ESO Hα 279a Revealed by NA I and CO Overtone Emission Lines. *The Astrophysical Journal* **844**, 4 (2017). URL https://ui.adsabs.harvard.edu/abs/2017ApJ...844....4L. Publisher: IOP ADS Bibcode: 2017ApJ...844....4L.

[11] D'Alessio, P., Calvet, N., Hartmann, L., Franco-Hernández, R. & Servín, H. Effects of Dust Growth and Settling in T Tauri Disks. *The Astrophysical Journal* **638**, 314–335 (2006). URL https://ui.adsabs.harvard.edu/abs/2006ApJ...638..314D. Publisher: IOP ADS Bibcode: 2006ApJ...638..314D.

[12] McClure, M. K. *et al.* Curved Walls: Grain Growth, Settling, and Composition Patterns in T Tauri Disk Dust Sublimation Fronts. *The Astrophysical Journal* **775**, 114 (2013). URL https://ui.adsabs.harvard.edu/abs/2013ApJ...775..114M. Publisher: IOP ADS Bibcode: 2013ApJ...775..114M.

[13] Cassen, P. Utilitarian Models of the Solar Nebula. *Icarus* **112**, 405–429 (1994). URL https://www.sciencedirect.com/science/article/pii/S001910358471195X.

[14] Woitke, P., Drażkowska, J., Lammer, H., Kadam, K. & Marigo, P. CAI formation in the early Solar System (2024). URL https://ui.adsabs.harvard.edu/abs/2024arXiv240415715W. Publication Title: arXiv e-prints ADS Bibcode: 2024arXiv240415715W.

[15] Do-Duy, T. *et al.* Crystalline silicate absorption at 11.1 m: ubiquitous and abundant in embedded YSOs and the interstellar medium. *Monthly Notices of the Royal Astronomical Society* **493**, 4463–4517 (2020). URL https://ui.adsabs.harvard.edu/abs/2020MNRAS.493.4463D. Publisher: OUP ADS Bibcode: 2020MNRAS.493.4463D.

[16] Poteet, C. A. *et al.* A Spitzer Infrared Spectrograph Detection of Crystalline Silicates in a Protostellar Envelope. *The Astrophysical Journal* **733**, L32 (2011). URL https://ui.adsabs.harvard.edu/abs/2011ApJ...733L..32P. Publisher: IOP ADS Bibcode: 2011ApJ...733L..32P.

[17] Davis, C. J., Stern, L., Ray, T. P. & Chrysostomou, A. Near-infrared Fabry-Perot imaging of Herbig-Haro energy sources: Collimated, small-scale H2 jets and wide-angled winds. *Astronomy and Astrophysics* **382**, 1021–1031 (2002). URL https://ui.adsabs.harvard.edu/abs/2002A&A...382.1021D. ADS Bibcode: 2002A&A...382.1021D.

[18] Vleugels, C., McClure, M., Sturm, A. & Vlasblom, M. The h2 jet and disk wind of the class i protostar hops 315. *AA* **695**, A145 (2025). URL https://doi.org/10.1051/0004-6361/202452475.

[19] Davis, C. J. *et al.* VLT integral field spectroscopy of embedded protostars: using near-infrared emission lines as tracers of accretion and outflow. *Astronomy and Astrophysics* **528**, A3 (2011). URL https://ui.adsabs.harvard.edu/abs/2011A&

A...528A...3D. ADS Bibcode: 2011A&A...528A...3D.

[20] Harsono, D. *et al.* JWST Peers into the Class I Protostar TMC1A: Atomic Jet and Spatially Resolved Dissociative Shock Region. *The Astrophysical Journal* **951**, L32 (2023). URL https://ui.adsabs.harvard.edu/abs/2023ApJ...951L..32H. Publisher: IOP ADS Bibcode: 2023ApJ...951L..32H.

[21] Tychoniec, *et al.* JWST Observations of Young protoStars (JOYS). Linked accretion and ejection in a Class I protobinary system. *Astronomy and Astrophysics* **687**, A36 (2024). URL https://ui.adsabs.harvard.edu/abs/2024A&A...687A..36T. ADS Bibcode: 2024A&A...687A..36T.

[22] Arulanantham, N. *et al.* JWST MIRI MRS Images of Disk Winds, Water, and CO in an Edge-on Protoplanetary Disk. *The Astrophysical Journal* **965**, L13 (2024). URL https://ui.adsabs.harvard.edu/abs/2024ApJ...965L..13A. Publisher: IOP ADS Bibcode: 2024ApJ...965L..13A.

[23] Pascucci, I. *et al.* The nested morphology of disk winds from young stars revealed by JWST/NIRSpec observations. *Nature Astronomy* (2024). URL https://ui.adsabs.harvard.edu/abs/2024NatAs.tmp..279P. ADS Bibcode: 2024NatAs.tmp..279P.

[24] Gail, H. P. & Sedlmayr, E. Mineral formation in stellar winds. I. Condensation sequence of silicate and iron grains in stationary oxygen rich outflows. *Astronomy and Astrophysics* **347**, 594–616 (1999). URL https://ui.adsabs.harvard.edu/abs/1999A&A...347..594G. ADS Bibcode: 1999A&A...347..594G.

[25] Dutta, S. *et al.* ALMA Survey of Orion Planck Galactic Cold Clumps (ALMASOP): Detection of a Dense SiO Jet in the Evolved Protostellar Phase. *The Astrophysical Journal* **925**, 11 (2022). URL https://ui.adsabs.harvard.edu/abs/2022ApJ...925...11D. Publisher: IOP ADS Bibcode: 2022ApJ...925...11D.

[26] Woitke, P. *et al.* 2D disc modelling of the JWST line spectrum of EX Lupi. *Astronomy and Astrophysics* **683**, A219 (2024). URL https://ui.adsabs.harvard.edu/abs/2024A&A...683A.219W. ADS Bibcode: 2024A&A...683A.219W.

[27] Vernazza, J. E., Avrett, E. H. & Loeser, R. Structure of the solar chromosphere. III. Models of the EUV brightness components of the quiet sun. *The Astrophysical Journal Supplement Series* **45**, 635–725 (1981). URL https://ui.adsabs.harvard.edu/abs/1981ApJS...45..635V. Publisher: IOP ADS Bibcode: 1981ApJS...45..635V.

[28] Petaev, M. I. & Wood, J. A. The condensation with partial isolation model of condensation in the solar nebula. *Meteoritics and Planetary Science* **33**, 1123–1137 (1998). URL https://ui.adsabs.harvard.edu/abs/1998M&PS...33.1123P. ADS Bibcode: 1998M&PS...33.1123P.

[29] Jorge, D. M., Kamp, I. E. E., Waters, L. B. F. M., Woitke, P. & Spaargaren, R. J. Forming Planets Around Stars With Non-Solar Elemental Composition. *Astronomy & Astrophysics* **660**, A85 (2022). URL https://www.aanda.org/articles/aa/abs/2022/04/aa42738-21/aa42738-21.html. Publisher: EDP Sciences.

[30] Gail, H. P. Radial mixing in protoplanetary accretion disks. IV. Metamorphosis of the silicate dust complex. *Astronomy and Astrophysics* **413**, 571–591 (2004). URL https://ui.adsabs.harvard.edu/abs/2004A&A...413..571G. ADS Bibcode: 2004A&A...413..571G.

[31] Komatsu, M. *et al.* First evidence for silica condensation within the solar protoplanetary disk. *Proceedings of the National Academy of Science* **115**, 7497–7502 (2018). URL https://ui.adsabs.harvard.edu/abs/2018PNAS..115.7497K. ADS Bibcode: 2018PNAS..115.7497K.

[32] Krot, A. N. Refractory inclusions in carbonaceous chondrites: Records of early solar system processes. *Meteoritics & Planetary Science* **54**, 1647–1691 (2019). URL https://onlinelibrary.wiley.com/doi/abs/10.1111/maps.13350. _eprint: https://onlinelibrary.wiley.com/doi/pdf/10.1111/maps.13350.

[33] Torrano, Z. A. *et al.* A common isotopic reservoir for amoeboid olivine aggregates (AOAs) and calcium-aluminum-rich inclusions (CAIs) revealed by Ti and Cr isotopic compositions. *Earth and Planetary Science Letters* **627**, 118551 (2024). URL https://www.sciencedirect.com/science/article/pii/S0012821X23005629.

[34] Sargent, B. A. *et al.* Dust Processing and Grain Growth in Protoplanetary Disks in the Taurus-Auriga Star-Forming Region. *The Astrophysical Journal Supplement Series* **182**, 477–508 (2009). URL https://ui.adsabs.harvard.edu/abs/2009ApJS..182..477S. Publisher: IOP ADS Bibcode: 2009ApJS..182..477S.

[35] Olofsson, J. *et al.* C2D Spitzer-IRS spectra of disks around T Tauri stars. IV. Crystalline silicates. *Astronomy and Astrophysics* **507**, 327–345 (2009). URL https://ui.adsabs.harvard.edu/abs/2009A&A...507..327O. ADS Bibcode: 2009A&A...507..327O.

[36] Wang, Y., Ormel, C. W., Mori, S. & Bai, X.-N. Solving for the 2D Water Snowline with Hydrodynamic Simulations. Emergence of gas outflow, water cycle and temperature plateau (2025). URL https://ui.adsabs.harvard.edu/abs/2025arXiv250208936W. Publication Title: arXiv e-prints ADS Bibcode: 2025arXiv250208936W.

[37] Faure, J., Fromang, S. & Latter, H. Thermodynamics of the dead-zone inner edge in protoplanetary disks. *Astronomy and Astrophysics* **564**, A22 (2014). URL https://ui.adsabs.harvard.edu/abs/2014A&A...564A..22F. ADS Bibcode: 2014A&A...564A..22F.

[38] Yang, L. & Ciesla, F. J. The effects of disk building on the distributions of refractory materials in the solar nebula. *Meteoritics & Planetary Science* **47**, 99–119 (2012). URL https://onlinelibrary.wiley.com/doi/abs/10.1111/j.1945-5100.2011.01315.x. _eprint: https://onlinelibrary.wiley.com/doi/pdf/10.1111/j.1945-5100.2011.01315.x.

[39] Shu, F. H., Shang, H. & Lee, T. Toward an Astrophysical Theory of Chondrites. *Science* **271**, 1545–1552 (1996). URL https://www.science.org/doi/10.1126/science.271.5255.1545. Publisher: American Association for the Advancement of Science.

[40] Morbidelli, A. *et al.* Formation and evolution of a protoplanetary disk: Combining observations, simulations, and cosmochemical constraints. *Astronomy & Astrophysics* **691**, A147 (2024). URL https://www.aanda.org/articles/aa/abs/2024/11/aa51388-24/aa51388-24.html. Publisher: EDP Sciences.

[41] Cridland, A. J. *et al.* Early planet formation in embedded protostellar disks. Setting the stage for the first generation of planetesimals. *Astronomy and Astrophysics* **662**, A90 (2022). URL https://ui.adsabs.harvard.edu/abs/2022A&A...662A..90C. ADS Bibcode: 2022A&A...662A..90C.

[42] McClure, M. K., Dominik, C. & Kama, M. Measuring the atomic composition of planetary building blocks. *Astronomy and Astrophysics* **642**, L15 (2020). URL https://ui.adsabs.harvard.edu/abs/2020A&A...642L..15M. Publisher: EDP ADS Bibcode: 2020A&A...642L..15M.

[43] Alexander, C. M. O. Quantitative models for the elemental and isotopic fractionations in the chondrites: The non-carbonaceous chondrites. *Geochimica et Cosmochimica Acta* **254**, 246–276 (2019). URL https://ui.adsabs.harvard.edu/abs/2019GeCoA.254..246A. ADS Bibcode: 2019GeCoA.254..246A.

[44] Grewal, D. S., Nie, N. X., Zhang, B., Izidoro, A. & Asimow, P. D. Accretion of the earliest inner Solar System planetesimals beyond the water snowline. *Nature Astronomy* **8**, 290–297 (2024). URL https://www.nature.com/articles/s41550-023-02172-w. Publisher: Nature Publishing Group.

[45] Scherstén, A., Elliott, T., Hawkesworth, C., Russell, S. & Masarik, J. Hf W evidence for rapid differentiation of iron meteorite parent bodies. *Earth and Planetary Science Letters* **241**, 530–542 (2006). URL https://ui.adsabs.harvard.edu/abs/2006E&PSL.241..530S. ADS Bibcode: 2006E&PSL.241..530S.

[46] Kleine, T. *et al.* Hf-W chronology of the accretion and early evolution of asteroids and terrestrial planets. *Geochimica et Cosmochimica Acta* **73**, 5150–5188 (2009). URL https://ui.adsabs.harvard.edu/abs/2009GeCoA..73.5150K. ADS Bibcode: 2009GeCoA..73.5150K.

[47] Tobin, J. J. *et al.* The VLA/ALMA Nascent Disk and Multiplicity (VANDAM) Survey of Orion Protostars. II. A Statistical Characterization of Class 0 and Class I Protostellar Disks. *The Astrophysical Journal* **890**, 130 (2020). URL https://ui.adsabs.harvard.edu/abs/2020ApJ...890..130T. Publisher: IOP ADS Bibcode: 2020ApJ...890..130T.

[48] Bushouse, H. *et al.* JWST Calibration Pipeline (2023).

[49] Argyriou, I. *et al.* JWST MIRI flight performance: The Medium-Resolution Spectrometer. *Astronomy and Astrophysics* **675**, A111 (2023). URL https://ui.adsabs.harvard.edu/abs/2023A&A...675A.111A. ADS Bibcode: 2023A&A...675A.111A.

[50] McMullin, J. P., Waters, B., Schiebel, D., Young, W. & Golap, K. CASA Architecture and Applications **376**, 127 (2007). URL https://ui.adsabs.harvard.edu/abs/2007ASPC..376..127M. Conference Name: Astronomical Data Analysis Software and Systems XVI ADS Bibcode: 2007ASPC..376..127M.

[51] Müller, H. S. P., Schlöder, F., Stutzki, J. & Winnewisser, G. The Cologne Database for Molecular Spectroscopy, CDMS: a useful tool for astronomers and spectroscopists. *Journal of Molecular Structure* **742**, 215–227 (2005).

[52] Ehrenfreund, P., Boogert, A. C. A., Gerakines, P. A., Tielens, A. G. G. M. & van Dishoeck, E. F. Infrared spectroscopy of interstellar apolar ice analogs. *Astronomy and Astrophysics* **328**, 649–669 (1997). URL https://ui.adsabs.harvard.edu/abs/1997A&A...328..649E. ADS Bibcode: 1997A&A...328..649E.

[53] Dominik, C., Min, M. & Tazaki, R. OpTool: Command-line driven tool for creating complex dust opacities. *Astrophysics Source Code Library* ascl:2104.010 (2021). URL https://ui.adsabs.harvard.edu/abs/2021ascl.soft04010D. ADS Bibcode: 2021ascl.soft04010D.

[54] Rocha, W. R. M. *et al.* LIDA: The Leiden Ice Database for Astrochemistry. **668**, A63 (2022).

[55] Kemper, F., Vriend, W. J. & Tielens, A. G. G. M. The Absence of Crystalline Silicates in the Diffuse Interstellar Medium. *The Astrophysical Journal* **609**, 826–837 (2004). URL https://ui.adsabs.harvard.edu/abs/2004ApJ...609..826K. Publisher: IOP ADS Bibcode: 2004ApJ...609..826K.

[56] Rocha, W. R. M., Perotti, G., Kristensen, L. E. & Jørgensen, J. K. Fitting infrared ice spectra with genetic modelling algorithms. Presenting the ENIIGMA fitting tool. **654**, A158 (2021).

[57] Burnham, K. & Anderson, D. *Model selection and multimodel inference: a practical information-theoretic approach* (Springer Verlag, 2002).

[58] Francis, L. *et al.* JOYS: MIRI/MRS spectroscopy of gas-phase molecules from the high-mass star-forming region IRAS 23385+6053. *Astronomy and Astrophysics* **683**, A249 (2024). URL https://ui.adsabs.harvard.edu/abs/2024A&A...683A.249F. ADS Bibcode: 2024A&A...683A.249F.

[59] Grant, S. L. *et al.* MINDS. The Detection of $^{13}CO_2$ with JWST-MIRI Indicates Abundant CO_2 in a Protoplanetary Disk. **947**, L6 (2023).

[60] Tabone, B. *et al.* A rich hydrocarbon chemistry and high C to O ratio in the inner disk around a very low-mass star. *Nature Astronomy* **7**, 805–814 (2023).

[61] KÃ³spÃ¡l, *et al.* JWST/MIRI Spectroscopy of the Disk of the Young Eruptive Star EX Lup in Quiescence. *The Astrophysical Journal* **945**, L7 (2023). URL https://ui.adsabs.harvard.edu/abs/2023ApJ...945L...7K. Publisher: IOP ADS Bibcode: 2023ApJ...945L...7K.

[62] Pontoppidan, K. M., Evans, N., Bergner, J. & Yang, Y.-L. A Constrained Dust Opacity for Models of Dense Clouds and Protostellar Envelopes. *Research Notes of the American Astronomical Society* **8**, 68 (2024). URL https://ui.adsabs.harvard.edu/abs/2024RNAAS...8...68P. Publisher: IOP ADS Bibcode: 2024RNAAS...8...68P.

[63] Foreman-Mackey, D., Hogg, D. W., Lang, D. & Goodman, J. emcee: The MCMC Hammer. *Publications of the Astronomical Society of the Pacific* **125**, 306 (2013). URL https://ui.adsabs.harvard.edu/abs/2013PASP..125..306F. Publisher: IOP ADS Bibcode: 2013PASP..125..306F.

[64] Carr, J. S., Tokunaga, A. T. & Najita, J. Hot H2O Emission and Evidence for Turbulence in the Disk of a Young Star. *The Astrophysical Journal* **603**, 213–220 (2004). URL https://ui.adsabs.harvard.edu/abs/2004ApJ...603..213C. Publisher: IOP ADS Bibcode: 2004ApJ...603..213C.

[65] Wilson, T. L. Isotopes in the interstellar medium and circumstellar envelopes. *Reports on Progress in Physics* **62**, 143–185 (1999). URL https://ui.adsabs.harvard.edu/abs/1999RPPh...62..143W. Publisher: IOP ADS Bibcode: 1999RPPh...62..143W.

[66] Thi, W. F., van Dishoeck, E. F., Pontoppidan, K. M. & Dartois, E. Evidence for episodic warm outflowing CO gas from the intermediate-mass young stellar object IRAS 08470-4321. *Monthly Notices of the Royal Astronomical Society* **406**, 1409–1424 (2010). URL https://ui.adsabs.harvard.edu/abs/2010MNRAS.406.1409T. Publisher: OUP ADS Bibcode: 2010MNRAS.406.1409T.

Extended Data Table 1 Results of `ENIIGMA` fitting to infrared solid state bands.

Name	Material	$N_{\rm solid}$ [$\times 10^{17}$ cm^{-2}]			
		M5(w)	M4(w)	M5(s)	M4(s)
Forsterite	Mg_2SiO_4	$1.3^{1.8}_{0.5}$	$1.2^{1.3}_{1.2}$	$2.0^{2.3}_{1.8}$	$1.4^{1.6}_{1.2}$
Enstatite	$MgSiO_3$	$3.7^{4.3}_{2.9}$	$4.8^{4.9}_{4.7}$	$4.1^{4.3}_{4.0}$	$4.4^{4.6}_{4.1}$
Silica	α-SiO_2	$1.4^{1.6}_{1.3}$	-	$2.7^{2.9}_{2.6}$	-
Interstellar	'GCS3'	17^{18}_{16}	18^{19}_{17}	16^{16}_{14}	18^{19}_{17}
Blended ice	H_2O	40^{42}_{38}	43^{44}_{41}	39^{40}_{37}	41^{42}_{39}
Blended ice	CO_2	$3.1^{3.3}_{2.9}$	$3.2^{3.3}_{3.1}$	$2.8^{2.9}_{2.7}$	$3.0^{3.1}_{2.9}$
$N_{enstatite}/N_{forsterite}$		$2.8^{8.6}_{1.6}$	$4.0^{4.1}_{3.6}$	$2.05^{2.4}_{1.7}$	$3.1^{3.8}_{2.6}$
χ^2_r		7.28	8.13	6.71	14.37
AIC		17.29	16.14	16.72	22.37

[a]The following minerals were included but found not to contribute to the fit at statistically significant levels: corundum (α-Al_2O_3, [1]), hibonite ($CaAl_{12}O_{19}$, [2]), gehlenite ($Ca_2Al_2SiO_7$, [3]), perovskite ($CaTiO_3$, [4]), spinel ($MgAl_2O_4$, [1]).

[b]Ice blend with H_2O:CO_2 (10:1)

[c]Five-component fit, with silica, 7.75-28 μm.

[d]Four-component fit, no silica, 7.75-28 μm.

[e]Five-component fit, with silica, 7.75-13.2 μm.

[f]Four-component fit, no silica, 7.75-13.2 μm.

[g]We report 3σ confidence intervals, not uncertainties.

Extended Data Table 2 Results of slab model fits to infrared molecular bands.

Molecule	λ [μm]	T [K]	N [cm^{-2}]	ΔV [km s^{-1}]	R [au]
Absorption					
SiO	7.8-8.6	472^{478}_{468}	$4.62^{4.76}_{4.48}\times10^{18}$	$13.4^{13.6}_{13.2}$	1.07-1.24
C_2H_2	13.7	715^{1092}_{490}	$5.93^{12.10}_{3.61}\times10^{15}$	$45.9^{80.4}_{14.4}$	0.09-0.10
HCN	14	517^{556}_{484}	$2.73^{2.98}_{2.50}\times10^{16}$	$58.1^{84.7}_{21.8}$	0.06-0.07
H_2O	2.7-3.0	401^{402}_{400}	$4.20^{4.23}_{4.17}\times10^{19}$	$24.4^{24.5}_{24.3}$	0.32-0.37
H_2O	5-7	443^{444}_{442}	$2.64^{2.66}_{2.62}\times10^{19}$	$20.6^{20.7}_{20.6}$	0.46-0.52
H_2O	15-17	524^{538}_{509}	$2.71^{3.27}_{2.31}\times10^{18}$	$4.53^{4.96}_{4.10}$	9.4-10.7
CO_2	4.2-4.4	351^{353}_{348}	$1.81^{1.84}_{1.78}\times10^{17}$	$23.6^{24.1}_{23.2}$	0.35-0.39
CO_2	14.7-15.5	124^{135}_{114}	$1.23^{2.36}_{0.66}\times10^{19}$	$3.51^{3.71}_{3.34}$	15.7-17.9
^{12}CO	4.4-5.1	1181^{1188}_{1174}	$7.39^{7.51}_{7.30}\times10^{18}$	$37.7^{38.1}_{37.4}$	0.14-0.15
^{13}CO	4.4-5.1	646^{665}_{627}	$9.14^{9.33}_{8.96}\times10^{17}$	$36.1^{38.9}_{33.7}$	0.15-0.17
Emission					
^{12}CO	2.29-2.4	3754^{3800}_{3710}	$2.40^{2.45}_{2.34}\times10^{21}$	fixed 37.7	$0.543^{0.551}_{0.535}$

[a]The range of disk radii for each absorption band, assuming disk Keplerian motion and no turbulence, for two limiting cases where z_{disk}/R_{disk}=0.2 and z_{disk}/R_{disk}=0, as motivated in Methods.

[b]The emission is de-reddened using $A_V = 38$ [5] with a theoretical extinction curve [6] suited for near-infrared correction. The emission band radius was fit with the models, assuming the same velocity as the ^{12}CO absorption component.

[c]These are 1σ confidence intervals.

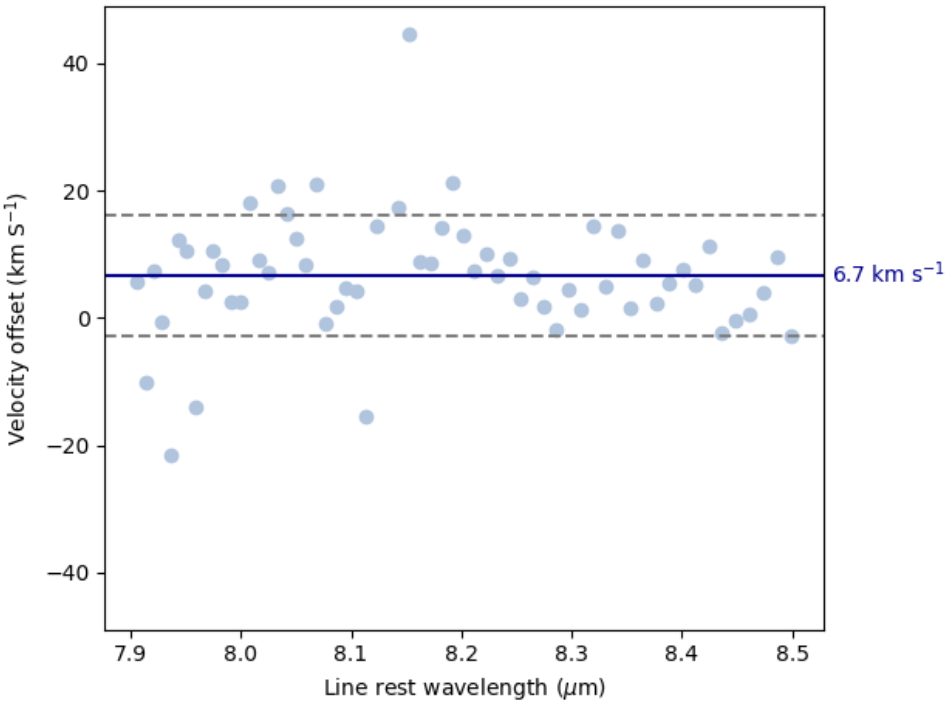

Extended Data Figure 1 Velocity offset of individual SiO $\nu = 1-0$ lines (circles) between 7.9 and 8.5 μm from their rest frame wavelength, as determined by a Gaussian fit. The mean velocity offset and mean plus or minus one standard deviation are shown by the dark blue and dashed horizontal lines, respectively. **The barycentric reference frame is offset from LSRK by -17.3** $km\ s^{-1}$**.**

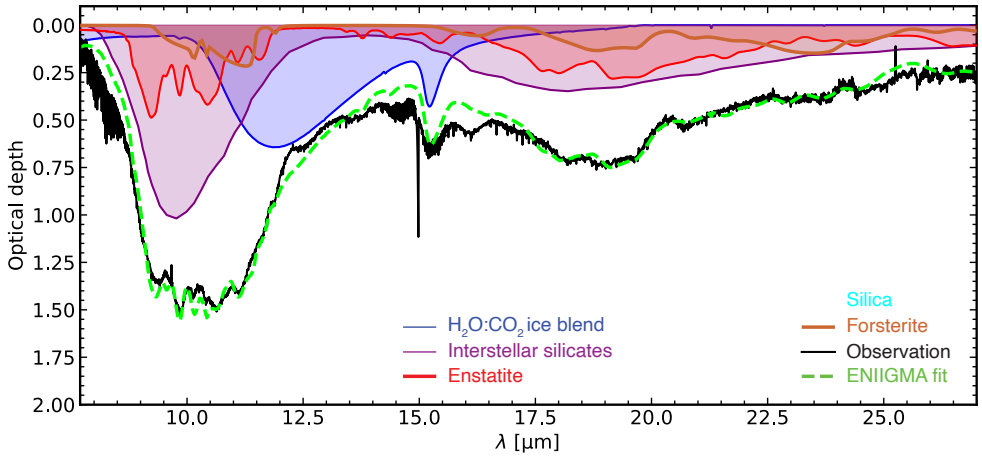

Extended Data Figure 2 `ENIIGMA` fit without silica over the whole wavelength range, M4(w).

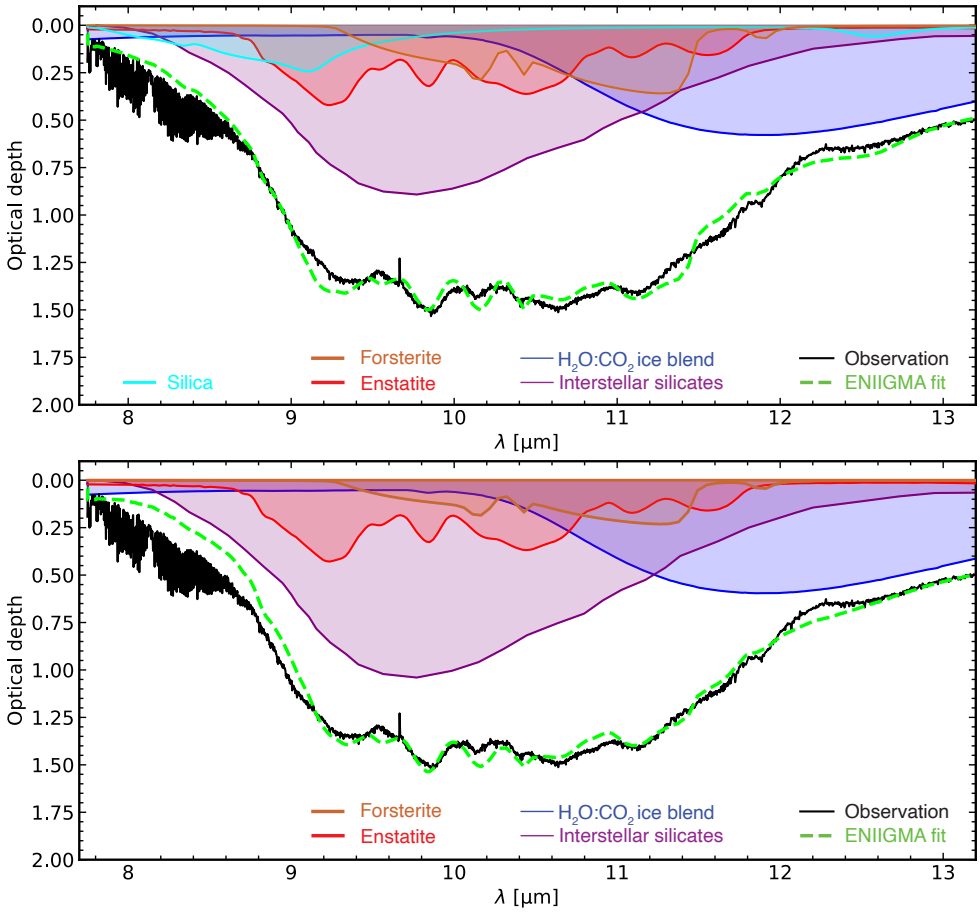

Extended Data Figure 3 `ENIIGMA` fit with silica (top panel, M5(s) model) and without silica (bottom panel, M4(s) model) over the 7.75-13.2 μm range. Silica improves the fit in a statistically significant way from 8-9 μm and at 12.5 μm.

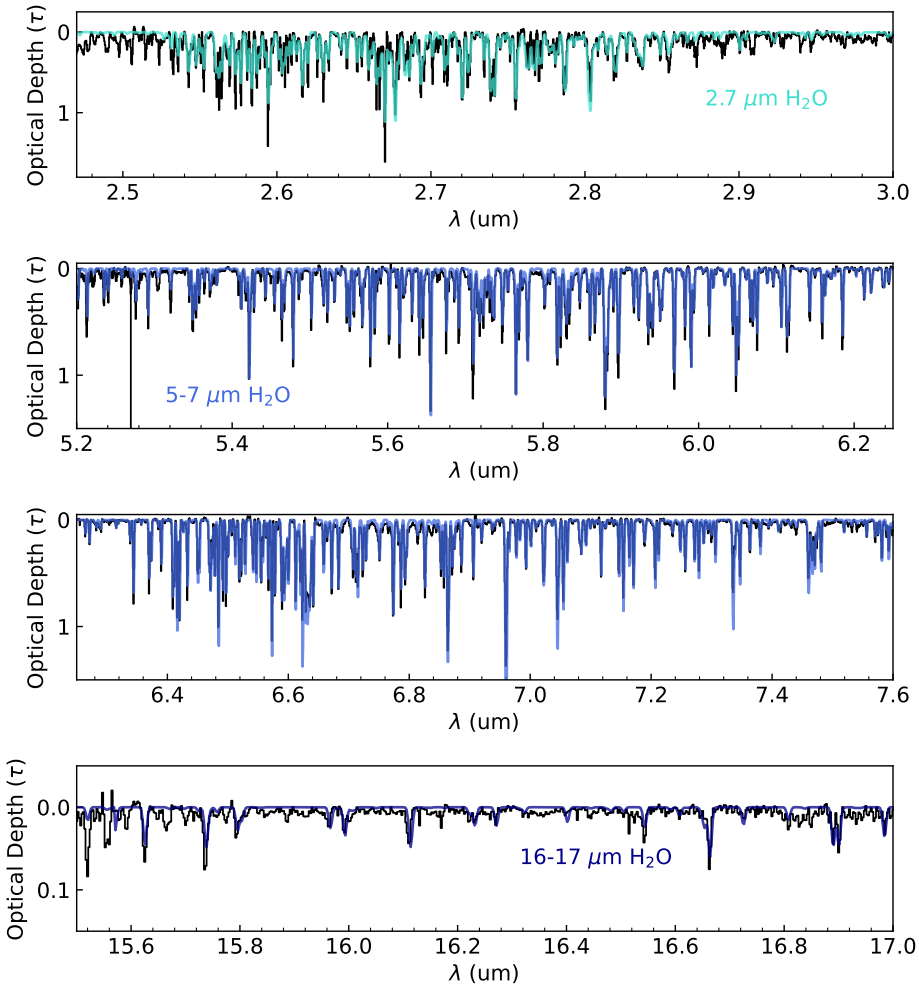

Extended Data Figure 4 Slab model fits to the H_2O gas phase absorption bands.

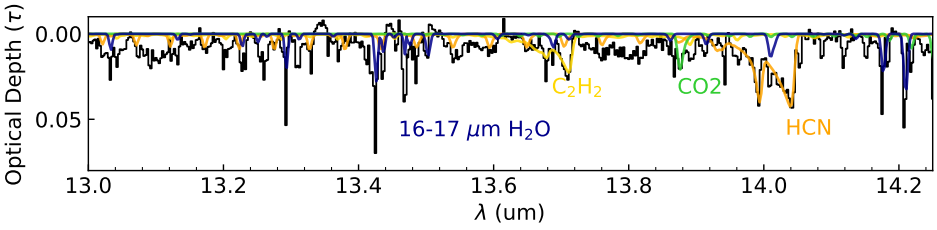

Extended Data Figure 5 Slab model fits to the C_2H_2 and HCN gas phase absorption bands.

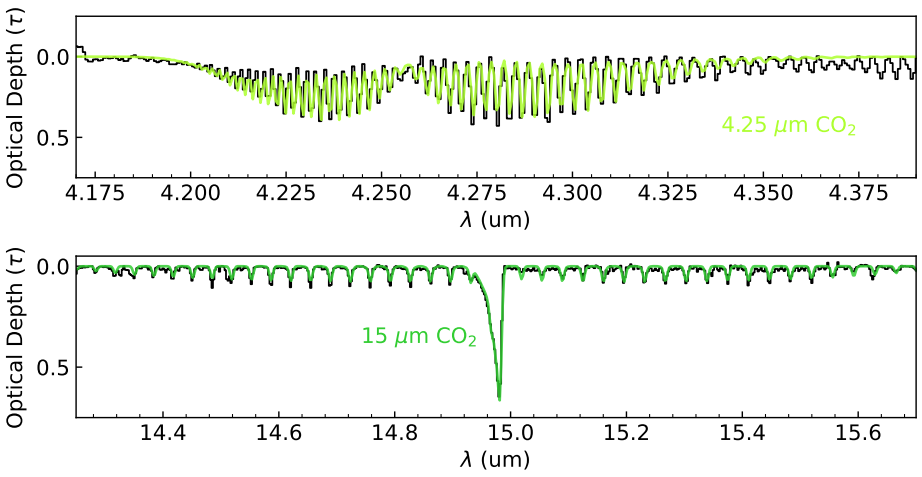

Extended Data Figure 6 Slab model fits to the CO_2 absorption bands. *Top panel:* The 4.27 μm band. *Bottom panel:* The 15.3 μm band.

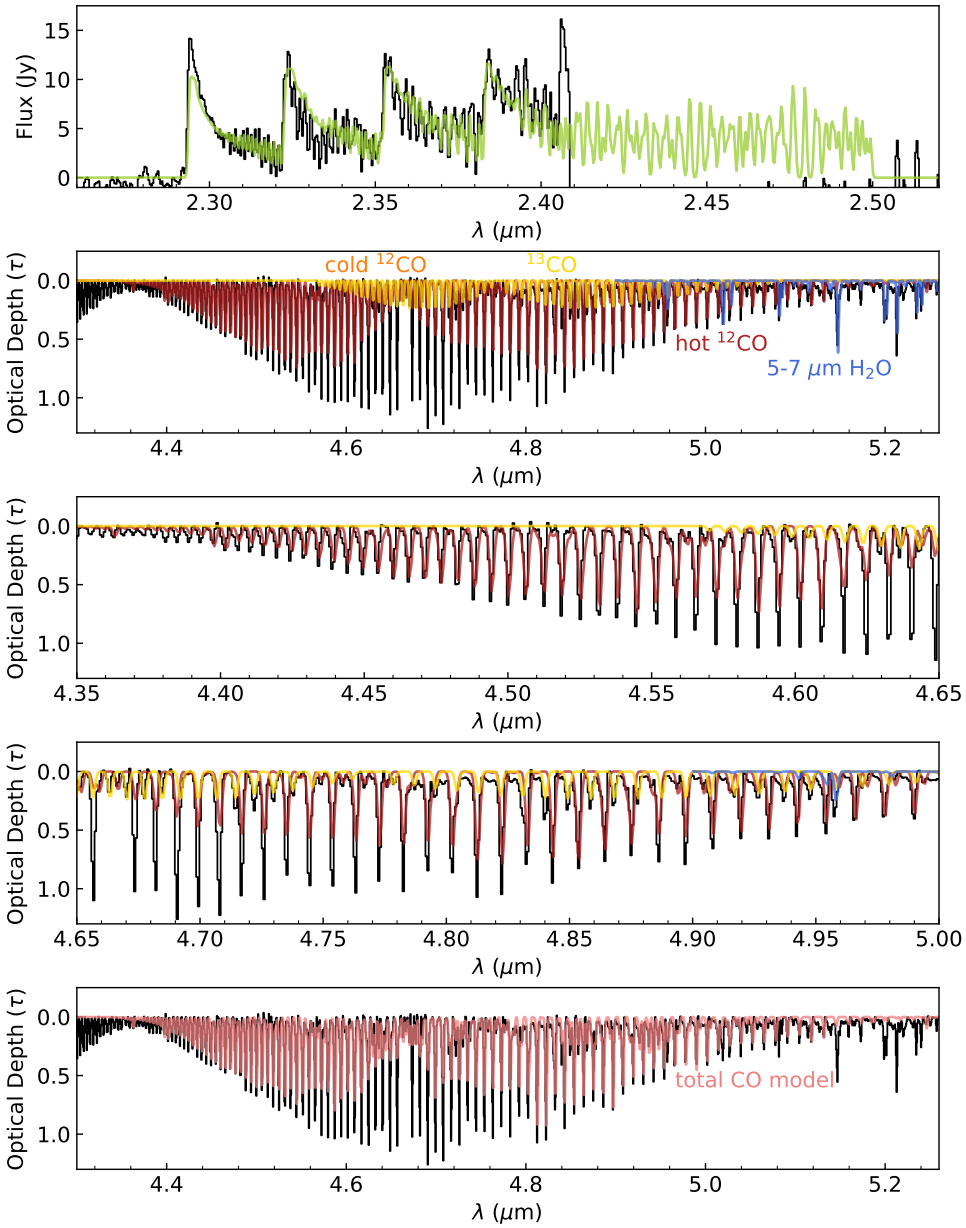

Extended Data Figure 7 Slab model fits for the CO vapor. *Top panel:* The overtone ν=2–0, 3–1 and 4–2 bands appear in emission and trace hot, dense gas above the temperature inversion layer. *Second panel:* The CO fundamental ν= 1-0 band shows at least three absorption components, of which we fit two: hot ^{12}CO and warm ^{13}CO components that trace the inner edge of the thermostat region. The residuals of these fits indicate a missing cold ^{12}CO component, with a more complex geometry than is appropriate for our model. *Third and fourth panels:* Zoom in on individual lines, to show the quality of the fit. *Last panel:* The sum of all three components, compared with the observational data. Residuals due to a cold component with a different covering fraction are discussed in Methods and Supplementary Methods Figure 13.

References

[1] Zeidler, S., Posch, T. & Mutschke, H. Optical constants of refractory oxides at high temperatures. Mid-infrared properties of corundum, spinel, and -quartz, potential carriers of the 13 m feature. *Astronomy and Astrophysics* **553**, A81 (2013). URL https://ui.adsabs.harvard.edu/abs/2013A&A...553A..81Z. ADS Bibcode: 2013A&A...553A..81Z.

[2] Mutschke, H., Posch, T., Fabian, D. & Dorschner, J. Towards the identification of circumstellar hibonite. *Astronomy & Astrophysics* **392**, 1047–1052 (2002). URL https://www.aanda.org/articles/aa/abs/2002/36/aah3747/aah3747.html. Number: 3 Publisher: EDP Sciences.

[3] Mutschke, H. *et al.* Steps toward interstellar silicate mineralogy. III. The role of aluminium in circumstellar amorphous silicates. *Astronomy and Astrophysics* **333**, 188–198 (1998). URL https://ui.adsabs.harvard.edu/abs/1998A&A...333..188M. ADS Bibcode: 1998A&A...333..188M.

[4] Posch, T. *et al.* Infrared Properties of Solid Titanium Oxides: Exploring Potential Primary Dust Condensates. *The Astrophysical Journal Supplement Series* **149**, 437–445 (2003). URL https://ui.adsabs.harvard.edu/abs/2003ApJS..149..437P. Publisher: IOP ADS Bibcode: 2003ApJS..149..437P.

[5] Davis, C. J. *et al.* VLT integral field spectroscopy of embedded protostars: using near-infrared emission lines as tracers of accretion and outflow. *Astronomy and Astrophysics* **528**, A3 (2011). URL https://ui.adsabs.harvard.edu/abs/2011A&A...528A...3D. ADS Bibcode: 2011A&A...528A...3D.

[6] Pontoppidan, K. M., Evans, N., Bergner, J. & Yang, Y.-L. A Constrained Dust Opacity for Models of Dense Clouds and Protostellar Envelopes. *Research Notes of the American Astronomical Society* **8**, 68 (2024). URL https://ui.adsabs.harvard.edu/abs/2024RNAAS...8...68P. Publisher: IOP ADS Bibcode: 2024RNAAS...8...68P.

Supplementary Methods

1 Error analysis for ENIIGMA solid state feature fitting.

To assess the quality of the fit including silica against a comparable `ENIIGMA` model without silica, we used the Root Mean Squared Error (RMSE), Akaike Information Criterion (AIC), and Reduced Chi-squared (χ_r^2) statistical metrics, defined below.

$$RMSE = \sqrt{\frac{\sum_{i=0}^{n-1}(O_i - M_i)^2}{n}} \tag{1}$$

where O_i and M_i are the observed and modelled data at each data point i, and N is the number of data points.

$$AIC = {\chi_r}^2 + 2p + \frac{2p(p+a)}{n-p-1}, \tag{2}$$

where p is the number of parameters and n is the number of bins. The ΔAIC is defined as AIC_i - $min(AIC)$, where AIC_i represent values for different models, and $min(AIC)$ corresponds to the minimum AIC value. ${\chi_r}^2$ is defined as

$$\chi_r^2 = \frac{1}{dof}\sum_{i=0}^{n-1}\left(\frac{\tau_{\lambda,i}^{\rm obs} - \sum_{j=0}^{m-1} w_j \tau_{\lambda,j}^{\rm model}}{\sigma_{\lambda,i}^{\rm obs}}\right)^2 \tag{3}$$

where dof is the number of degrees of freedom, σ is the error in the observational optical depth, n is the number of data points, λ is the wavelength, $\tau_{\lambda,\rm i}^{\rm obs}$ is the optical depth of the observational spectrum, $\tau_{\lambda,\rm j}^{\rm model}$ is the optical depth of the laboratory data, and w_j is the scaling factor.

For our preferred M5(w) model with silica, we calculated the confidence intervals of each dust component using `ENIIGMA`. This calculation performs a linear variation around the coefficients (w_j) in the best fit, and calculates new χ_r^2 values aiming to create a $\Delta\chi^2$ map. Supplementary Figure 1 shows the corner plots of each component. The green, yellow and red contours are the 1σ, 2σ, and 3σ confidence intervals. In this M5(w) fit, the 3σ confidence intervals are never below 0, even for silica, which indicates that all components improve the fit.

As discussed in the Main text, the M5(w) model (Figure 3) has χ^2_r=7.28 and AIC=17.29, while the M4(w) model (Extended Data Figure 2) has χ^2_r=8.13 and AIC=16.14. According to [1], a decrease of more than 2 in the AIC is required to consider one model statistically better than the other. In that sense, over the whole wavelength range silica is not required. However, when we fit both models to a reduced wavelength range of 7.75-13.2 μm (Extended Data Figure 3), then the model with silica, M5(s), has χ^2_r=6.71 and AIC=16.72, while the model without silica, M4(s), has χ^2_r=14.37 and AIC=22.37. In this case, the AIC decreases by 5.65, so the model with silica is statistically significantly better fit to the 10 μm complex.

2 Corner plots from slab model error analysis.

We include below the corner plots from the slab model analysis showing the interdependence of the temperature, column density, and ΔV parameters of the model fit (Supplementary Figures 2-12). In each case, there are 1, 2, and 3 σ confidence intervals overplotted. For the case of the CO fundamental band, we show the residuals after subtraction our model fits (Supplementary Figure 11). As described in the main text, these can be attributed to cold ^{12}CO that likely has a different covering fraction than the hot ^{12}CO or warm ^{13}CO components.

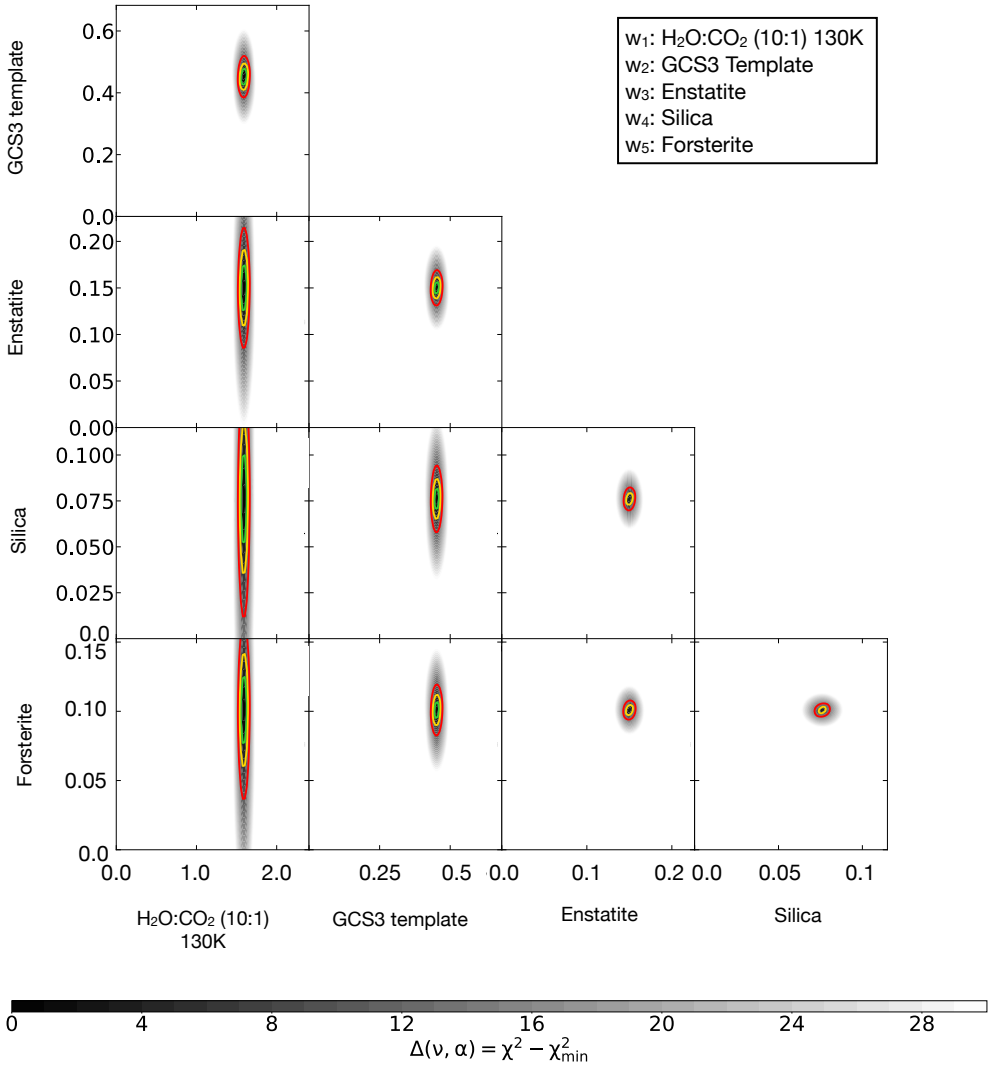

Supplementary Figure 1 Confidence intervals for the `ENIIGMA` fit with silica over the whole wavelength range, M5(w).

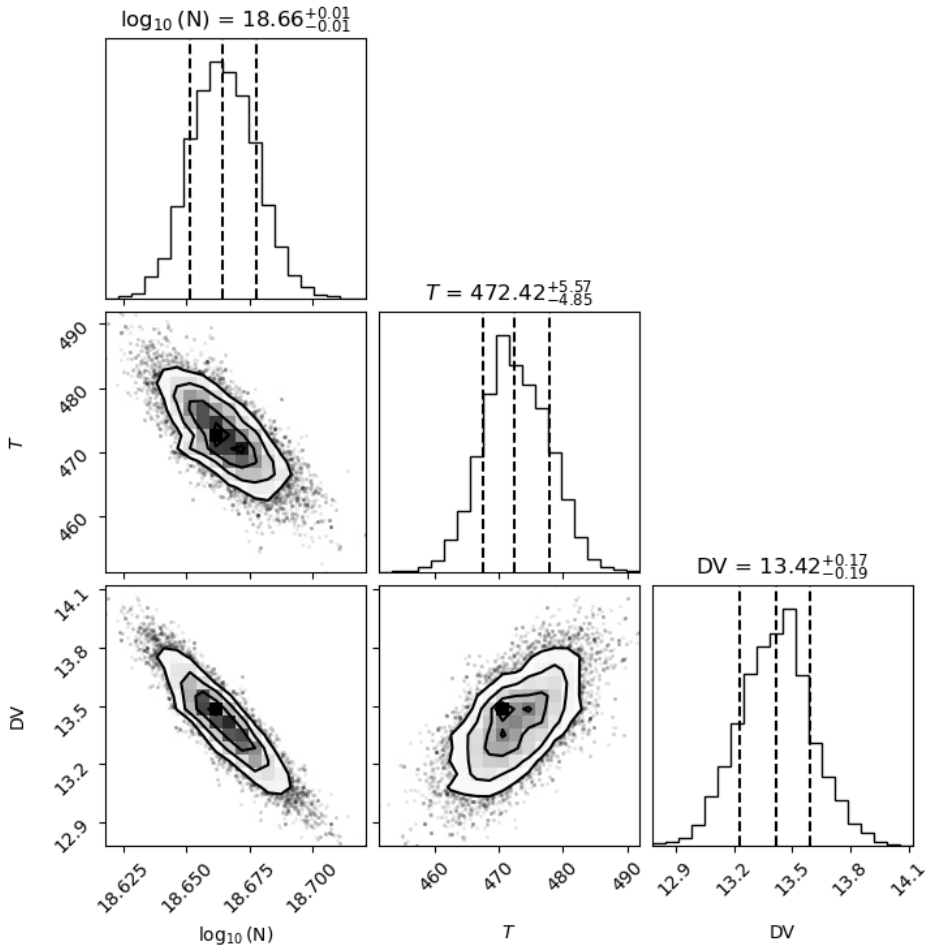

Supplementary Figure 2 Corner plot for SiO showing the interdependence of the three fitting parameters.

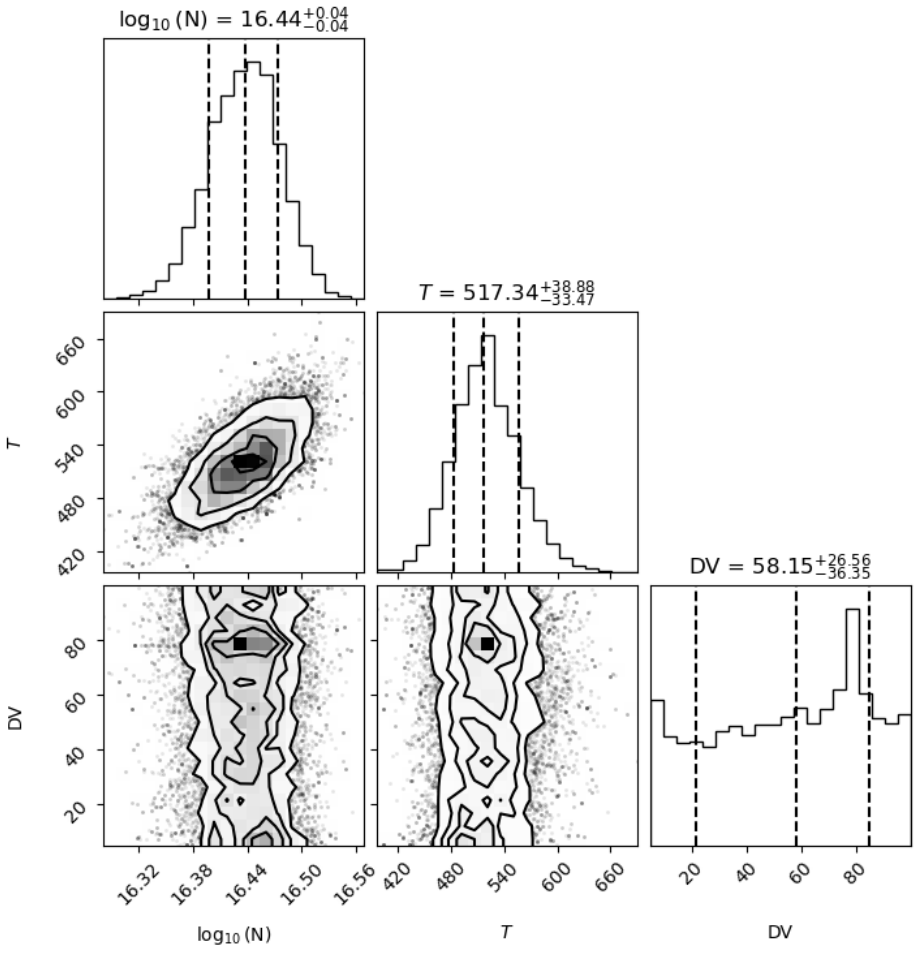

Supplementary Figure 3 Corner plot for HCN showing the interdependence of the three fitting parameters.

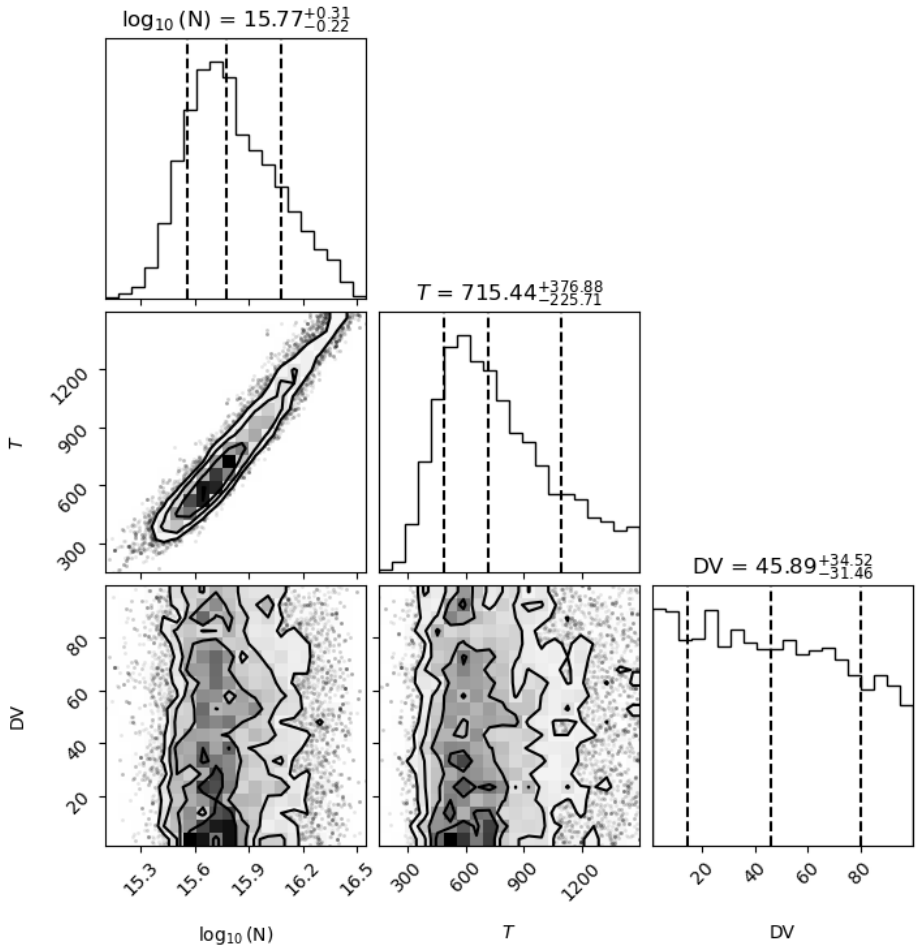

Supplementary Figure 4 Corner plot for C2H2 showing the interdependence of the three fitting parameters.

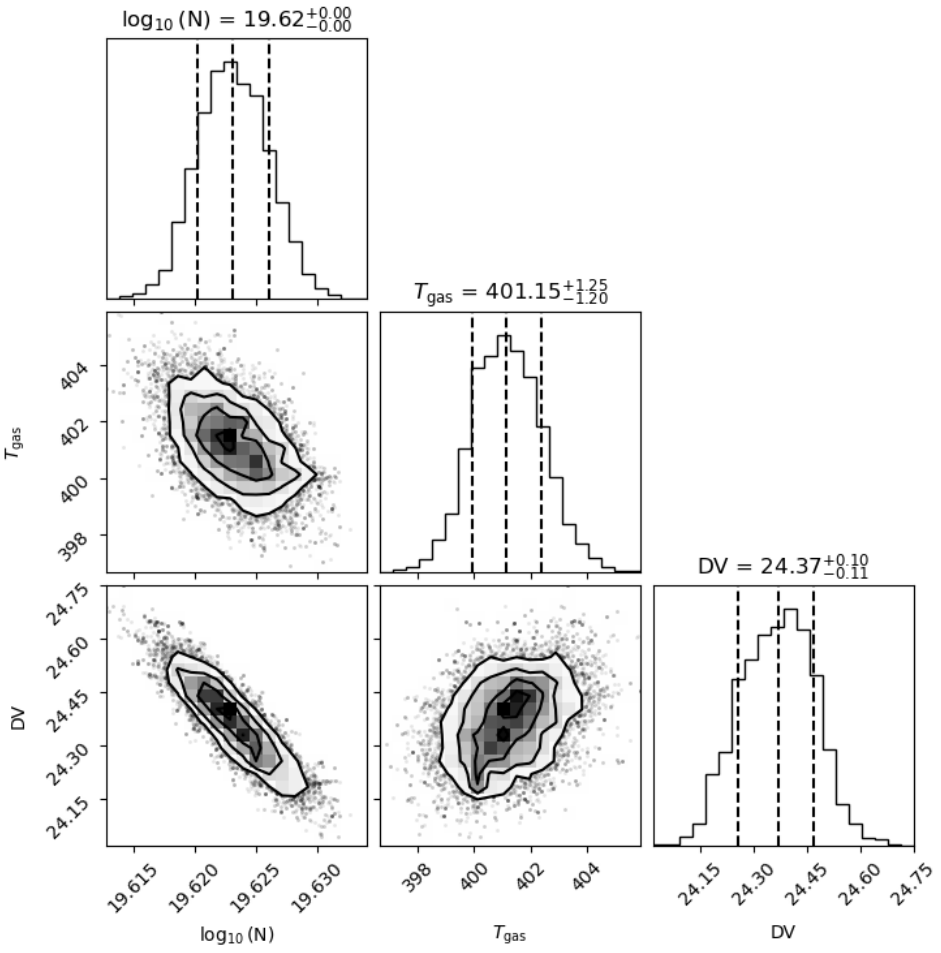

Supplementary Figure 5 Corner plot for 3 μm H_2O showing the interdependence of the three fitting parameters.

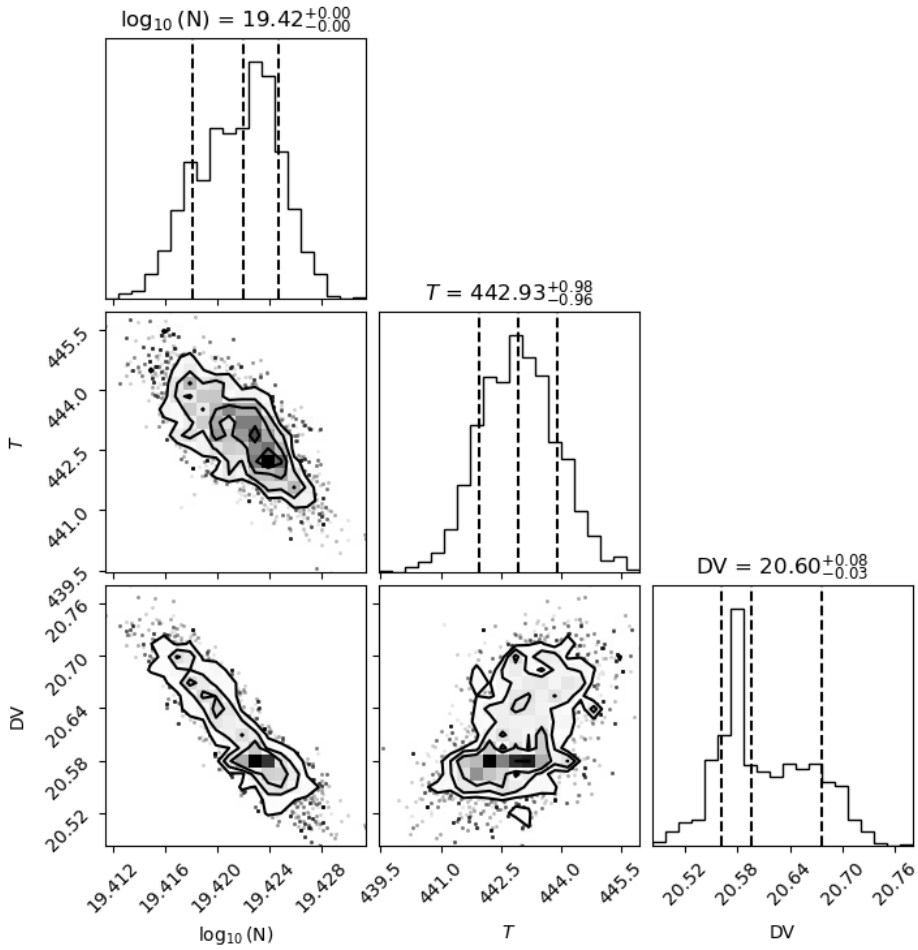

Supplementary Figure 6 Corner plot for 5-7 μm H_2O showing the interdependence of the three fitting parameters.

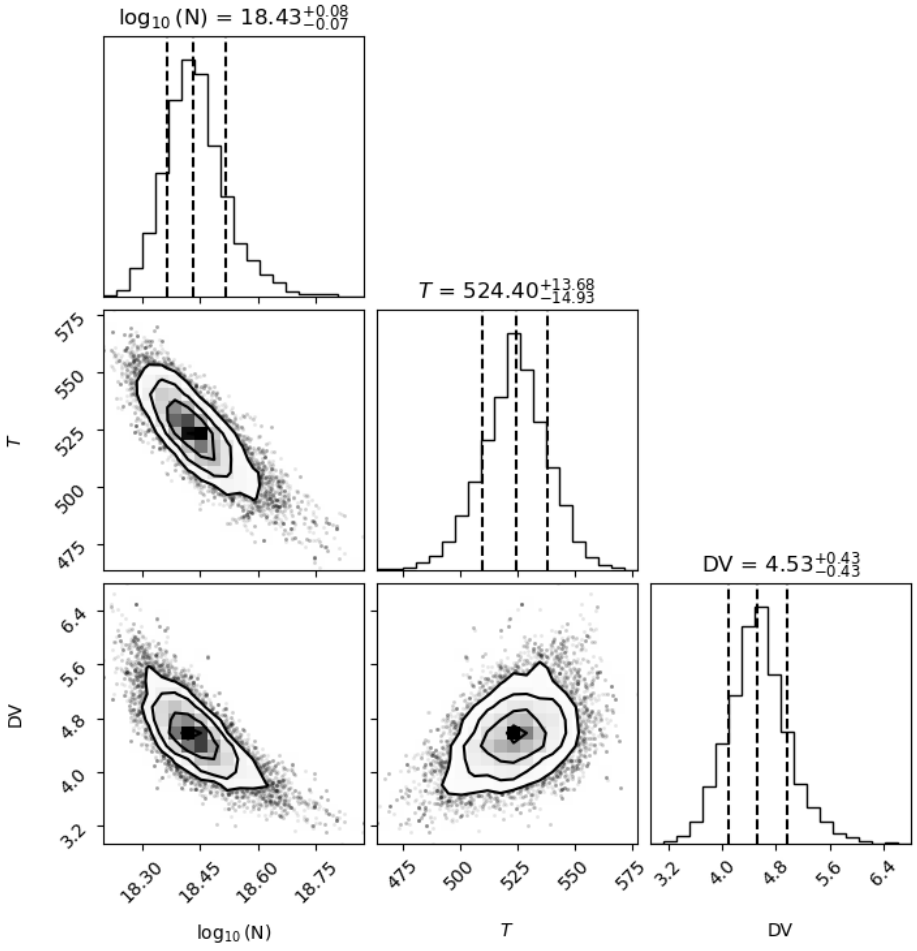

Supplementary Figure 7 Corner plot for 17 μm H_2O showing the interdependence of the three fitting parameters.

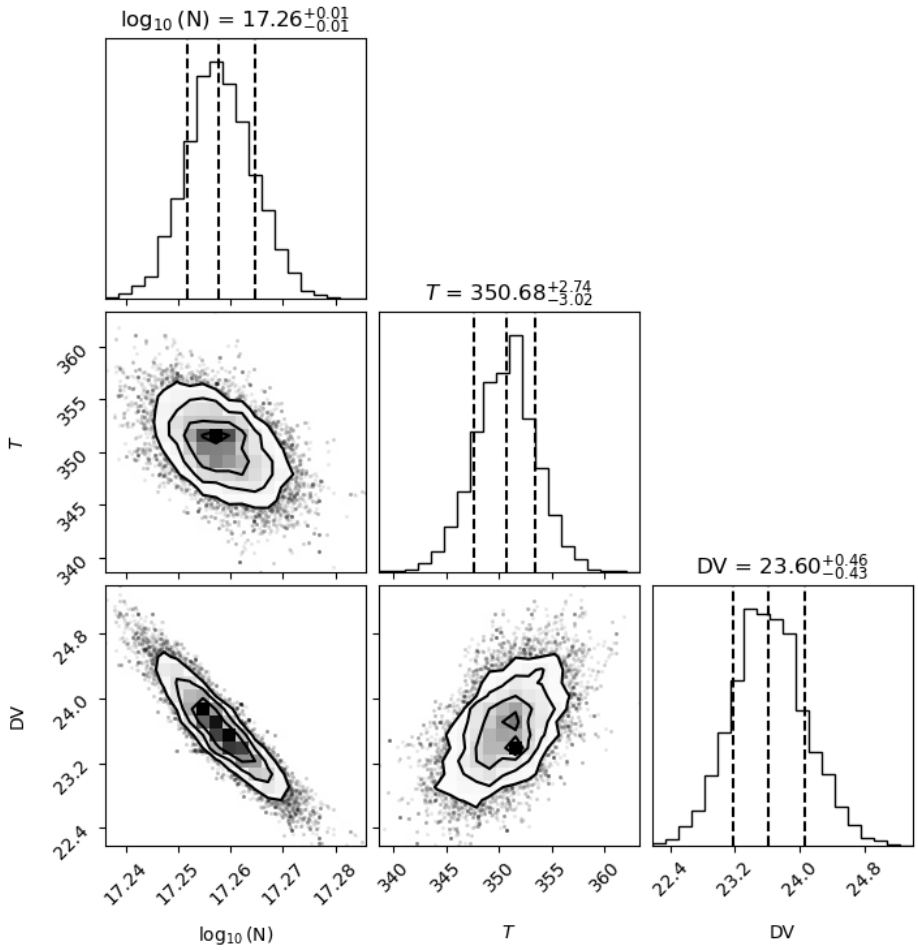

Supplementary Figure 8 Corner plot for 4.3 μm CO_2 showing the interdependence of the three fitting parameters.

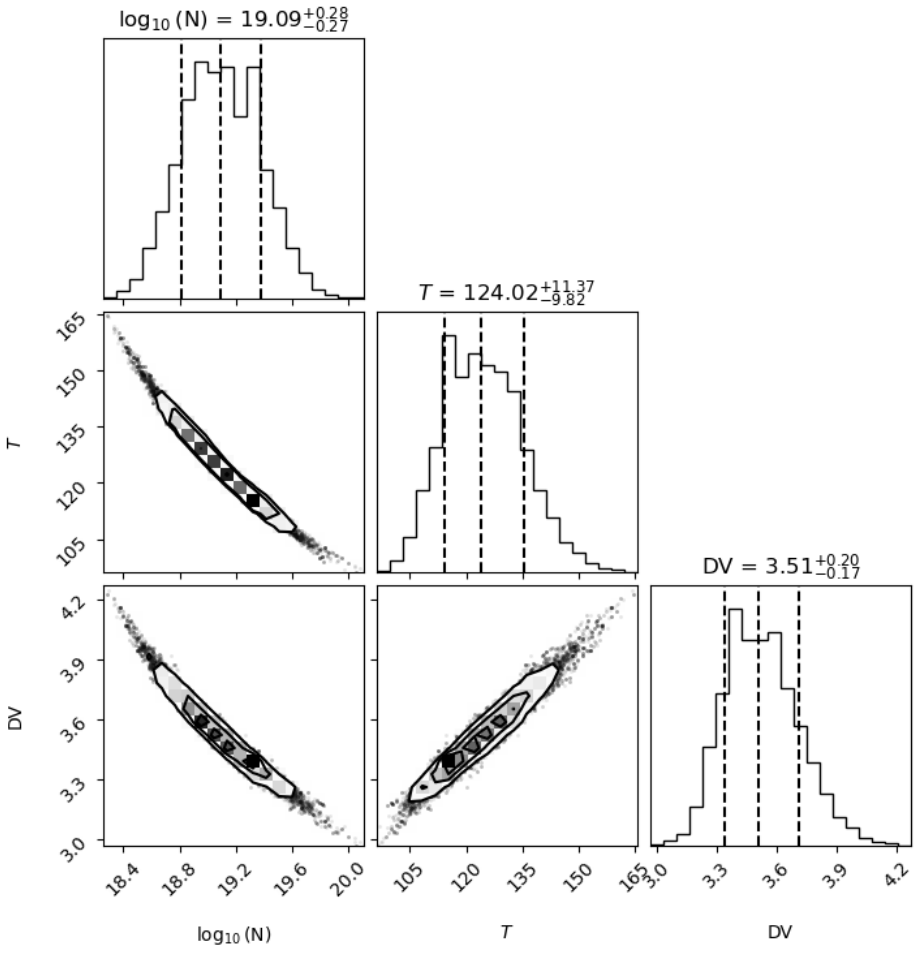

Supplementary Figure 9 Corner plot for 15 μm CO_2 showing the interdependence of the three fitting parameters.

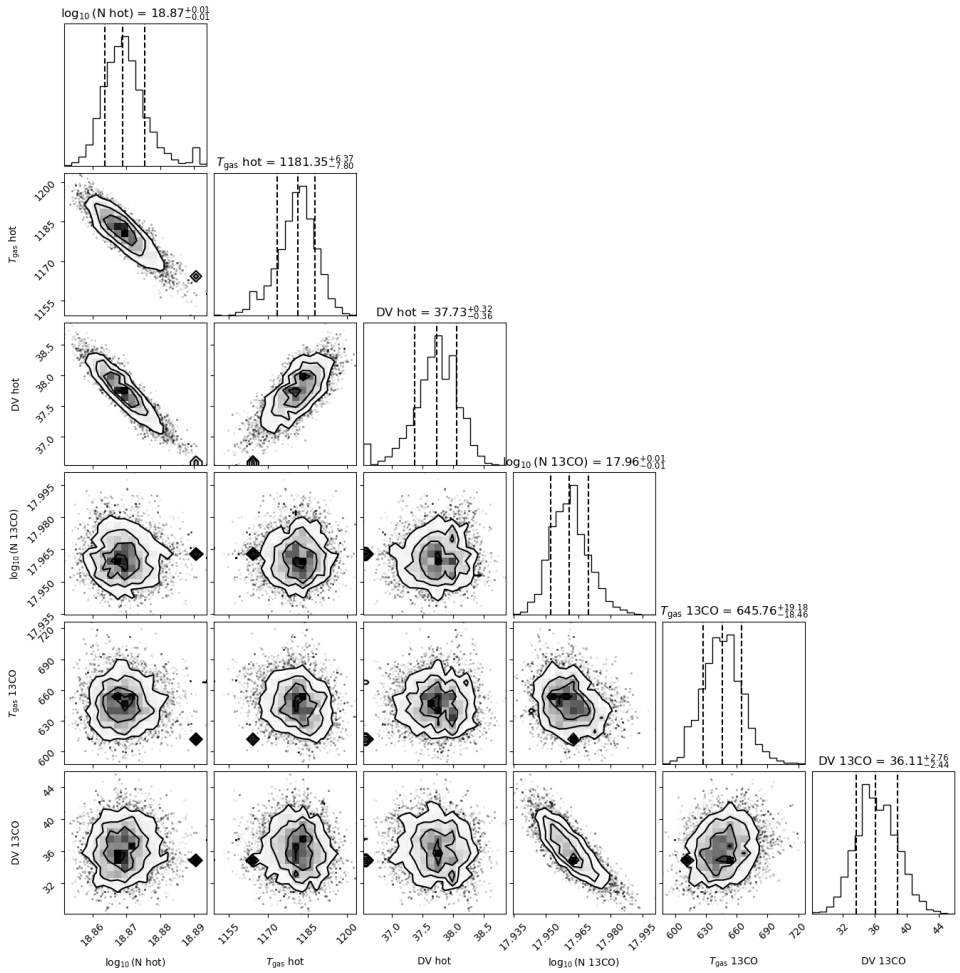

Supplementary Figure 10 Corner plot for 4.7 μm CO showing the interdependence of the three fitting parameters for ^{12}CO and ^{13}CO.

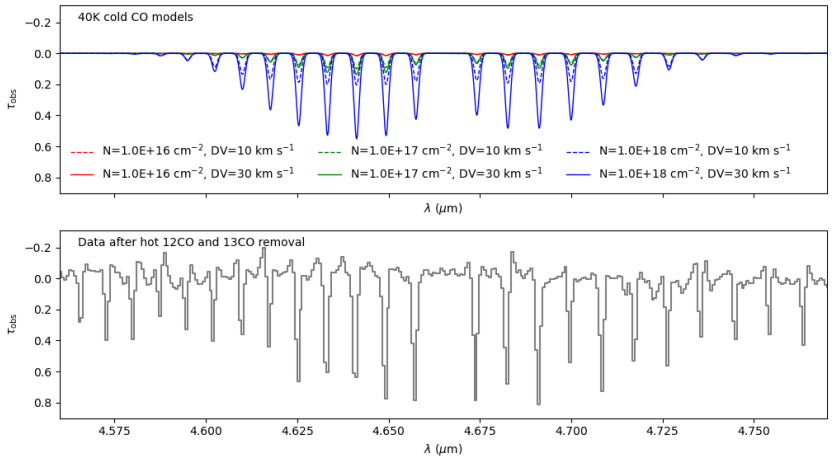

Supplementary Figure 11 Top. Models for cold, 40 K, ^{12}CO absorption with different values for ΔV. Residuals after subtraction of the warm ^{12}CO and ^{13}CO fit from the 4.7 μm CO band.

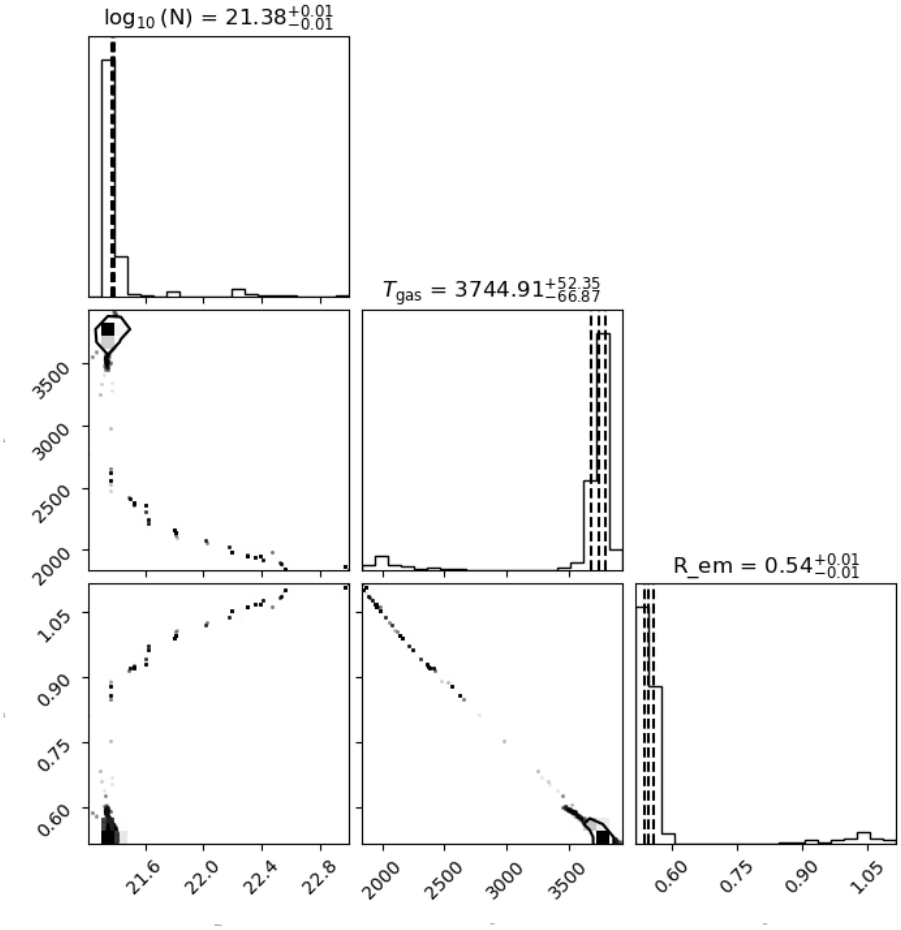

Supplementary Figure 12 Corner plot for 2.3 μm CO overtone showing the interdependence of the three fitting parameters.

References

[1] Burnham, K. & Anderson, D. *Model selection and multimodel inference: a practical information-theoretic approach* (Springer Verlag, 2002).